ON THE INTERNAL STRUCTURE QUANTIFICATION FOR GRANULAR CONSTITUTIVE MODELLING

Xia Li [a *]

[a] Department of Chemical and Environmental Engineering, Faculty of Engineering, University Park, The University of Nottingham, Nottingham, NG7 2RD, UK

ABSTRACT

The importance of internal structure on the stress-strain behavior of granular materials has been widely recognized. How to define the fabric tensor and to use it in constitutive modelling however remains an open question. The definition of fabric tensor requires 1) identifying the key aspects of structure information and 2) quantifying their impact on material strength and deformation. This paper addresses these issues by applying the homogenisation theory to interpret the multi-scale data obtained from the discrete element simulations. Numerical experiments have been carried out to test granular materials with different particle friction coefficients. More frictional particles tend to form less but larger void cells, leading to a larger sample void ratio. Upon shearing, they form more significant structure anisotropy and support higher force anisotropy, resulting in higher friction angle. Material strength and deformation have been explored on the local scale with the particle packing described by the void cell system. Three groups of fabric tensor have been covered in this paper. The first one is based on the contact vectors, which is the geometrical link between contact forces and material stress. And their relationship with material strength has been quantified by the Stress-Force-Fabric relationship. The second group is based on as the statistics of individual void cell characteristics. Material dilatancy has been interpreted by tracing the void cell statistics during shearing. The

* Corresponding author. Address: Department of Chemical and Environmental Engineering, Faculty of Engineering, University Park, University of Nottingham, Nottingham, NG7 2RD, United Kingdom, Email: xia.li@nottingham.ac.uk. Tel: +44(0)1159514167. Fax: +44(0)1159513898.

last group is based on the void vectors, for their direct presence in the micro-structural strain definition, including those based on the void vector probability density and mean void vector.

Correlations among various fabric quantifications have been explored. The mean void vector length and the mean void cell area are parameters quantifying the internal structure size, and strongly correlated with each other. Anisotropy indices defined based on contact normal density, void vector density, void vector length and void cell orientation are found effective in characterizing loading-induced anisotropy. They are also closely correlated. In-depth investigation on structural topology may help establish the correlation among different fabric descriptors and unify the fabric tensor definition. Deformation bands have been observed to continuously form, develop and disappear over a length scale of several tens of particle diameters. Its relation to and impact on material deformation is an area of future investigation.

Keywords: Fabric quantification, Granular statistics, Homogenisation theory, Discrete Element Method (DEM).

INTRODUCTION

Different from metal, the complexity in the stress-strain behaviour of granular materials is largely rooted in the packing formation and evolution upon shearing. It is widely acknowledged that the fabric tensor needs to be introduced into constitutive modelling to capture the main features of granular material behaviour. A number of fabric definitions have been proposed (Satake 1982, Oda 1985, Li and Li 2009, Nguyen, Magoariec et al. 2009, Kruyt and Rothenburg 2014). Generally speaking, the appropriateness of fabric definition depends on its application. Targeting at constitutive modelling, this paper interprets the material strength and deformation from the local scale in order to shed some light on the important and yet to answer questions, including 1) what is the most appropriate fabric definition used for modelling the material stress-strain behaviour and 2) how to effectively incorporate it to reflect the impact of internal structure on the material stress-strain responses.

Among many interesting earlier discoveries, (Satake 1978)'s graph-theoretical approach is instrumental in establishing the correspondence between discrete and continuum representations and informing the advancement of homogenisation theory. (Satake 1983) replaced an assembly of grains with graphs and formulated the mathematical expressions of discrete granular mechanics. The importance of voids has been recognized and emphasized by introducing dual particles to represent void spaces. In line of Satake's pioneering work, (Bagi 1996) introduced the concepts of two dual cell systems as the geometric representation of discrete assemblies, and building upon it, the duality of the stress and strain. (Li and Li 2009) extended the concept to three dimensional spaces by modifying the Voronoi-Delaunay tessellation systems with consideration of whether the particles are in real contact or not. In two dimensional spaces, their dual cell systems are equivalent to Satake's dual graphs. Interestingly, the idea of describing the material internal structure with a tessellation system has also been developed, though separately, in the field of granular statistics by (Blumenfeld and Edwards 2006). Instead of using two dual systems, they represent the granular structure with a set of grain polygons and void polygons.

With the internal structure described by the dual graphs or its analogues, the continuum scale stress tensor has been expressed in terms of particle interactions and contact vectors which are geometrical quantities in the solid cell system connecting contact points and particle centres. This correspondence has been theoretically established on Newton's second law of motion (Christoffersen 1981, Rothenburg and Selvadurai 1981, Bagi 1996, Kruyt and Rothenburg 1996, Li, Yu et al. 2009). In parallel, the continuum-scale strain tensor has been expressed in terms of particle relative displacements and geometrical quantities in the void cell systems based on the compatibility condition (Bagi 1996, Kruyt and Rothenburg 1996, Kuhn 1999, Li, Yu et al. 2009). The importance of internal structure is self-evident with the presence of local geometrical quantities in these two discrete expressions.

These theoretical developments in the homogenization theory have also laid down the groundwork to systematically investigate how the internal structure impacts on the stress-strain behavior from the local scale. In this study, numerical experiments have been carried out using the Discrete Element Method (DEM) (Cundall and Strack 1979) to provide the multi-scale data. A series of numerical simulations have been carried out on granular assemblies with identical particle geometries but different friction coefficients. The void cell system has been constructed to describe particle packing, and the continuum-scale material behavior is considered as the collective response from all individual void cells. Discussions have been extended to the definition of fabric tensor, which serves as a necessary state variable in constitutive modelling (Li and Dafalias 2012).

NUMERICAL SIMULATIONS

Numerical experiments have been carried out using the commercial package, Particle Flow Code (PFC2D), a two dimensional Discrete Element Method (DEM) software (Itasca Consulting Group Inc. 1999). The boundary control algorithm introduced in (Li, Yu et al. 2013) has been used to impose the target loading path. The particles are circular disks uniformly distributed in number within the range of (0.1mm, 0.3mm). The thickness of particles is set as 0.2 mm. The particle interactions are of linear stiffness with a slider. The normal and tangential stiffnesses are set as 1.0×10^5 N/m. A series of simulations have been carried out with the particle friction coefficient μ_p being 0.0, 0.1, 0.2, 0.5, 1.0 and 10.0 respectively. The specimens are hexagonal except for the case of $\mu_p = 10.0$, when the contact sliding is nearly prohibited, extremely large contact forces have been observed around the corner indicating local strong arching formation. The dodecagonal sample shape is hence used. The boundary properties are set as the same as the particle properties.

Figure 1 Void ratio prior to shearing vs particle friction coefficient

The samples are prepared using the deposition method. Particles are generated in a rectangular region whose height is twice the width. The particles deposit vertically at gravity $G = 100\text{m/s}^2$ in the low damping environment to form the initial packing, which is then trimmed by the prescribed boundary and consolidated to $p_c = 1000\text{kPa}$ for shearing. The scaled gravity is used to reduce computational time. Such prepared samples are expected to be initially anisotropic, although as shown later, of limited magnitude. For the series of numerical experiments carried out in this study, the numbers of particles range from 3,443 to 3,938 depending on the particle friction coefficient. The ratio between the sample size and the particle diameter is around 60, and is believed to be large enough to serve as representative elements. Due to the difference in particle friction coefficients, different initial structures are formed. Fig. 1 plots the void ratio of the samples, an index of packing density, at their initial (pre-shearing) states, which is observed to increase with the increase in particle friction coefficient. The packing with $\mu_p = 10.0$ has a similar void ratio to the packing with $\mu_p = 1.0$. This information is not included in the figure for better illustration of the variation when the friction coefficient varies between 0 and 1.

In analogy to drained tests, samples are sheared in the vertical direction while the mean normal pressures $p = (\sigma_1 + \sigma_2)/2$ are kept constant. The boundary control algorithm detailed in (Li, Yu et al. 2013) has been used to control the displacements of boundary walls synchronously to impose the strain-controlled boundary, and to monitor the stress boundary using a servo-controlled mechanism. Local damping has been used to dissipate excess kinetic energy during shearing. Loading increments are only imposed when both the equilibrium criteria and the specimen boundary conditions are satisfactorily met. The material responses are shown in Fig. 2 by plotting the stress ratio $\eta = q / p = 2(\sigma_1 - \sigma_2)/(\sigma_1 + \sigma_2)$ and the volumetric strain ε_v against the deviatoric strain ε_q, where σ_1 and σ_2 are the major and minor principal stresses respectively in two dimensional spaces. The stress ratio is related to material frictional angle as $\eta = 2\sin\phi$.

Figure 2 Material responses to shearing (a) Stress ratio b) Void ratio

The deposition method is expected to produce loose specimens. Most of the samples show strain hardening behavior however strain softening response has been observed in samples with high particle friction coefficients $\mu_p = 1.0$ and $\mu_p = 10.0$. The friction angles are observed to be low in general because circular particles have been used in the simulations. Similar to the observations in (Peyneau and Roux 2008), the sample made of frictionless particles ($\mu_p = 0.0$) exhibits a low shear resistance and little volume change. It flows nearly as a fluid, with the sample friction angle as low as 4.6^{o}. A very low and fluctuating volumetric strain up to 0.2% is observed. The sample frictional angle increases gradually to 14^{o} when the particle friction coefficient increases to 0.2. However, further increase in particle friction coefficient doesn’t further increase the material shear resistance. This is consistent with the laboratory (Skinner 1969) and numerical (Thornton 2000, Antony and Sultan 2007, Huang, Hanley et al. 2014) observations on 3D granular materials. The volume change exhibits more diversity. When the particle friction coefficient increases from 0 to 0.2, the sample becomes more contractive with the volumetric strain with $\mu_p = 0.2$ going up to 1%. However, when the particle friction coefficient increases further to $\mu_p = 0.5$, the sample contracts slightly and then behaves dilative. Further increase in particle friction coefficient leads to more dilative behavior with the volumetric strain with $\mu_p = 10.0$ as high as 2.8%. It is also observed that although the variation in stress ratio occurs mainly in the first 10% deviatoric strain, the change in volumetric strain continues until much larger strain levels.

FABRIC QUANTIFICATION PERTINENT TO MATERIAL SHEAR RESISTANE

The external loading is transmitted throughout the specimen via the force-bearing structure. Fig. 3 plots the force chains at the initial states. The heterogeneity in particle interaction is clear from the figure. It is observed that strong forces appear periodically over every few particle diameters. Since the chosen sample size is much larger than the dimension exhibited in force heterogeneity, the samples are considered as representative elements for stress analyses. Comparing Fig.3(a) & (b), samples of higher particle friction coefficients exhibit a periodicity over a slightly larger length scale.

Figure 3 Contact force distribution prior to shearing (a) $\mu_g = 0.0$ and (b) $\mu_g = 1.0$. (The thickness of the black lines is proportional to the magnitude of contact forces)

The Stress-Force-Fabric Relationship

Granular materials are known for its ability to self-organize their internal structure. Anisotropy develops as a result of shearing and makes an important contribution to material shear resistance. This section addresses the fabric quantification pertinent to the shear resistance of granular material in aid of the Stress-Force-Fabric relationship, which was originally proposed by (Rothenburg and Bathurst 1989). It was established based on the micro-structural definition of stress tensor, linking the continuum scale stress tensor σ_{ij} with contact forces f_i^c and contact vectors v_i^c as:

$$\sigma_{ij} = \frac{1}{V}\sum_{c \in V} v_i^c f_j^c \qquad (1)$$

in which V stands for the volume of interest. Note that a contact point is identified only when there is non-zero interaction between two entities. At an internal contact point between two particles, there is always a pair of action and reaction forces corresponding to two contact vectors pointing from the contact point to each particle centre. They are counted as two contacts. However, an external contact point between particle and boundary wall is only counted once.

(Li and Yu 2013) employed the theory of directional statistics (Kanatani 1984) to investigate the statistics of particle-scale information, characterised the directional dependence of particle-scale information with direction tensors and formulated the Stress-Force-Fabric relationship in the tensorial form. The notations used in (Li and Yu 2013, Li and Yu 2014) are followed in this paper. Examination of the particle-scale statistics supports the following simplifications:

1) There is a slight and isotropic statistical dependence between contact forces and contact vectors which can be approximated by $\left\langle v_i f_j \right\rangle|_{\mathbf{n}} = \varsigma \left\langle v_i \right\rangle|_{\mathbf{n}} \left\langle f_j \right\rangle|_{\mathbf{n}}$ where ς is a scalar around 1.025 for all the simulations. In this expression, $*|_{\mathbf{n}}$ denotes the value of variable * in direction $\mathbf{n}$, and $\langle * \rangle|_{\mathbf{n}}$ denotes the average value of all terms of $*$ sharing the same direction $\mathbf{n}$;
2) The contact vector length is isotropic;
3) The contact normal probability density can be sufficiently accurately approximated by up to the 2nd rank polynomial series of unit directional vector $\mathbf{n}$;
4) The mean contact force $\langle \mathbf{f} \rangle|_{\mathbf{n}}$ can be sufficiently accurately approximated by up to the 3rd rank polynomial series of unit directional vector $\mathbf{n}$.

Eq. (1) can be converted into integration over direction by grouping the terms with the same contact normal directions together. Combined with the above observations, the simplified Stress-Force-Fabric relationship can be written as:

$$\sigma_{ij} = \frac{\omega^p N^p}{2V} \varsigma v_0 f_0 \left[(1+h)\delta_{ij} + G_{ji}^f + \frac{1}{2} D_{ij}^c + G_{ij}^v \right] \quad (2)$$

where ω^p is the particle coordination number, N^p is the number of particles, v_0 is the directional average of mean contact vector and f_0 is the directional average of mean contact force, h is a scalar accounting for the contribution from the joint products which increases slightly from 0 to around 0.01 during shearing. In two dimensional spaces, the direction tensor for contact normal density is $D_{ij}^c = d^c \begin{pmatrix} \cos\phi^c & \sin\phi^c \\ \sin\phi^c & -\cos\phi^c \end{pmatrix}$, where d^c denotes the magnitude of directional variation and $\phi^c/2$ indicates the preferred principal direction of contact normal density. $G_{ij}^f = B^f \begin{pmatrix} \cos\beta^f & \sin\beta^f \\ \sin\beta^f & -\cos\beta^f \end{pmatrix}$ is the 2nd rank tensor characterizing the directional dependence of contact forces, where B^f denotes the magnitudes of directional variation, β^f indicates its preferable principal direction. It is worth pointing that G_{ij}^f covers the contributions from both the normal contact force components and the tangential contact force components. G_{ij}^c is defined similar to G_{ij}^f but characterises the statistics of contact vectors.

Approximation using Eq. (2) has been found to give exact matches of the continuum-scale stress, and provides a valid point to interpret material strength from the particle scale.

Fabric quantification

The micro-structural stress definition given in Eq. (1) shows that the particle-scale geometrical information linked to the material stress is contact vectors. And the SFF relationship given as Eq. (2) provides the analytical relationship quantifying the correlation between the contact vectors and material stress state. Considering the different nature in the normal and tangential force-displacement relationship, the terms in Eq. (1) has been grouped based on their contact normal directions, and the deviatoric tensor D_{ij}^c in Eq. (2) reflects the anisotropy in contact normal density. The anisotropy in contact vector is a secondary factor which can be characterized in terms of G_{ij}^{c}. These two aspects can be combined and quantified in terms of one fabric tensor. This section summarises their definitions and calculations based on directional statistical theories.

Fabric quantification for contact normal density

Contact normal based fabric tensor is one of the most widely used index in characterizing the loading induced anisotropy (Oda, Nemat-Nasser et al. 1985), and appears in Eq. (2) as $D_{ij}^{c} = d^{c}\begin{pmatrix} \cos\phi^{c} & \sin\phi^{c} \\ \sin\phi^{c} & -\cos\phi^{c} \end{pmatrix}$, which is called the fabric tensor of the third kind (Kanatani 1984). It describes the variation of contact normal density over direction. An equivalent definition is the fabric tensor of the second kind F_{ij}^{c} (Kanatani 1984). With them, the contact normal density distribution can be approximated as:

$$E^{c}(\mathbf{n}) = \frac{1}{E_0} F_{ij}^{c} n_i n_j = \frac{1}{E_0}\left(1 + D_{ij}^{c} n_i n_j\right) \tag{3}$$

where $E_0 = \oint_{\Omega} d\Omega = 2\pi$ in the two dimensional spaces. D_{ij}^{c} and F_{ij}^{c} are interchangeable as

$$F_{ij}^{c} = D_{ij}^{c} + \delta_{ij} \tag{4}$$

They can be determined from the fabric tensor of the first kind, also referred to the moment tensor N_{ij}^{c} in (Kanatani 1984, Li and Yu 2013) as $F_{ij}^{c} = 4\left(N_{ij}^{c} - \frac{1}{4}\delta_{ij}\right)$ and $D_{ij}^{c} = 4\left(N_{ij}^{c} - \frac{1}{2}\delta_{ij}\right)$, where the moment tensor can be calculated as:

$$N_{ij}^{c} = \left\langle n_i n_j \right\rangle = \frac{1}{M}\sum_{\alpha=1}^{M} n_i^{\alpha} n_j^{\alpha} \tag{5}$$

where $\mathbf{n}^{(1)}$, $\mathbf{n}^{(2)}$, $\cdots$ and $\mathbf{n}^{(N)}$ being the unit vectors representing contact normals. M is the total number of contacts.

Fabric quantification for contact vector anisotropies

The anisotropy in mean contact vector could be an additional contributor to material stress ratio as listed in the Stress-Force-Fabric relationship, Eq. (2), for non-spherical particles (Li and Yu 2014), although its anisotropy magnitude is often found to be secondary compared with that of contact normal density. The mean contact vector $\left\langle v_j \right\rangle|_{\mathbf{n}}$ can be approximated as $\left\langle v_j \right\rangle|_{\mathbf{n}} = v_0 \left(n_j + G_{ji}^c n_i \right)$, or equivalently in terms of the fabric tensor $H_{ij}^c = v_0 \left(1 + G_{ij}^c \right)$, where v_0 is the directional average of mean contact vector.

Fabric quantification combining contact normal and contact vector anisotropies

A combined account for the contribution of material fabric to stress state may include both contact normal density and contact vector anisotropy, and be defined on the contact vector based moment tensor as:

$$L_{ij}^c = \left\langle v_i n_j \right\rangle = \frac{1}{M} \sum_{\alpha=1}^{M} v_i^{\alpha} n_j^{\alpha} \approx \oint_{\Omega} E^c(\mathbf{n}) \left\langle v_i \right\rangle|_{\mathbf{n}} \, n_j d\Omega \tag{6}$$

Substituting Eq. (3) into Eq.(6) leads to $L_{ij}^c = v_0 \left[\frac{1}{2} \left(\delta_{ij} + G_{ij}^c \right) + \frac{1}{4} \left(D_{ij}^c + D_{im_1}^c G_{jm_1}^c \right) \right]$ in 2D spaces. Note D_{ij}^c and G_{ij}^c are deviatoric tensors. Neglecting the joint products of higher rank terms for simplicity and denoting the normalized deviator tensor as $C_{ij}^c = {2L_{ij}^c}/{L_{kk}^c} - \delta_{ij} = G_{ij}^c + D_{ij}^c/2$, the Stress-Force-Fabric relationship can be rewritten as:

$$\sigma_{ij} = \frac{\omega^p N^p}{2V} \varsigma v_0 f_0 \left(\delta_{ij} + C_{ij}^c + G_{ji}^f \right) \tag{7}$$

where $L_{ii}^c = v_0$. C_{ij}^c provides an explicit account of the impact of internal structure on material strength.

The micromechanical interpretation of material shear resistance

In this study, disk-shaped particles are used. The mean contact vector has been found nearly isotropic so that $G_{ij}^{c}=0$ and $C_{ij}^{c}=D_{ij}^{c}/2$. For all the simulations, the principal fabric directions are the same as the loading direction, and the material anisotropy can be characterized in terms of the degrees of contact normal anisotropy d^{c}, which is plotted in Fig. 4(a). Even for frictionless particles, shearing results in structure anisotropy, although of limited magnitude. More significant fabric anisotropy develops in more frictional particles. Upon shearing, the contact normal anisotropy increases mostly monotonically, although in more frictional samples, its rate of increases is observed to be higher and reaches a stronger anisotropy at the critical state. When the friction coefficient increases further beyond $\mu_{p}=0.5$, the evolutions of contact normal anisotropy are observed to no longer change. This is similar to the observation made in (Huang, Hanley et al. 2014) based on 3D DEM simulations.

Figure 4 The micro-mechanical contributors to material strength (a) Contact normal anisotropy d^{c}, and (b) Contact force anisotropy B^{f}

Information on contact force anisotropy B^{f} is plotted in Fig. 4(b). While particle friction coefficient increases, both the contact normal anisotropy and the contact force anisotropy increase. The contact force anisotropy however exhibits a peak before approaching the critical state, coincident with the occurrences of peak stress ratio followed by strain softening. It is interesting to point out that no matter what the particle friction coefficient is, the anisotropy in contact force is of similar magnitude with contact normal anisotropy, which is better shown in Fig. 5 by plotting the two anisotropies against each other. The reference line indicates when the two anisotropic degrees are equal to each other. The strong correlation between the contact normal anisotropy and the contact force anisotropy is evident with most data points falling near the reference line. Shearing motivates contact force anisotropy slightly faster and higher than the developed contact normal anisotropy. For samples made of very rough particles, contact force anisotropy was observed to be higher than the contact normal anisotropy at the early stage of shearing. When approaching the critical state, the two anisotropies become equal.

Figure 5 Correlation between the fabric and contact force anisotropy

In a summary, SFF relationship supports the effectiveness of D_{ij}^{c} and C_{ij}^{c} as the fabric tensor definition to study the material stress and hence strength. The force anisotropy is found strongly associated with the observed fabric anisotropy, in particular at the critical state. Hence, material shear strength can be determined from the fabric anisotropy should there be an established fabric-force correlation.

VOID CELL STATISTICS AND MATERIAL DILATANY

In this section, the relationship between material dilatancy and the evolution of void cell statistics will be explored by viewing a granular assembly as a collection of void cells. The void cell system is formed by connecting contact points and particle centres. Particles without contribution to the global force transmission, including those with few than two contact points, are excluded during the void cell construction. The number of constitutie particles in void cells should be no less than 3. Fig. 6 provides an example by presenting the void cell system with $\mu_p = 0.5$. The color scheme is associated with the void cell area. The void cells between boundary particles and walls have been identified in order to tessellate the whole space enclosed by the specimen boundaries.

Figure 6 The void cell system at pre-shearing stage ($\mu_p = 0.5$)

Void cell characterisation and void cell based fabric tensor

Viewing a granular material as an assembly of void cells, the material fabric tensor can be defined as the statistical average of individual void cell characteristics. The loop tensors used in (Nguyen, Magoariec et al. 2009, Kruyt and Rothenburg 2014) are such examples. However, there is no unique way in doing so. Here, the individual void cell is characterized based on the area moment of inertia, and the void cell based fabric tensor is proposed as their statistical average as one example of its kinds.

Characterisation of individual void cells

Void cells may have different and irregular shapes. A single dimension is inadequate to describe the geometry of individual void cells. Factors of primary interest are the size of the void cell, its shape and the orientation. The area moment of inertia $I_{ij} = \oint_A r_i r_j dA$, where r_i is the vector from the location of the area element dA to the area centre of void cell, contains all the necessary information and can be potentially used. Based on the area moment of inertia I_{ij}, the tensor Z_{ij} is used to describe the local cell geometry:

$$Z_{ij} = \frac{4}{A} I_{ij} \qquad (8)$$

Its principle direction gives information on the void cell orientation.

Figure 7 $\pi\sqrt{\det\left(Z_{ij}\right)}$ vs. void cell area

In the case of an ellipse of semi-major axis of length a and semi-minor axis of length b, $Z_{ij} = \begin{pmatrix} a^2 & 0 \\ 0 & b^2 \end{pmatrix}$. Note that the area of the ellipse is $\pi ab = \pi\sqrt{J(\mathbf{Z})} = \pi\sqrt{\det\left(Z_{ij}\right)}$, where $J(\mathbf{Z}) = \det\left(Z_{ij}\right)$ denotes the Jacobian determinant of tensor Z_{ij}. This suggests that

$\pi\sqrt{\det\left(Z_{ij}\right)}$ may serve as an effective estimation of void cell areas. Fig. 7 plots $\pi\sqrt{\det\left(Z_{ij}\right)}$ against the area of void cells for all the void cells shown in Fig. 6. The red line in the figure plots the reference line $y = x$. Despite their irregular shape, the data have been found lying closely to, with most data slightly above, the reference line.

The shape of an ellipse can be described by the index $(a-b)/(a+b)$. For a circle, the index is equal to 0 and for an ellipse with infinite aspect ratio, it is 1. In terms of the tensor defined in Eq.(8), the equivalent expression is the void cell anisotropy index $\Delta^v = \left(\sqrt{Z_1/Z_2}-1\right)/\left(\sqrt{Z_1/Z_2}+1\right)$, where Z_1 and Z_2 are the major and minor principal values of the fabric tensor Z_{ij}. Fig. 8 presents information on the shape of void cells by plotting the probability density function $d\,P|_{\Delta^v \le x}/d\Delta^v$, where $P|_{\Delta^v \le x}$ represents the probability of void cells whose shape factor Δ^v is no larger than x , and $d\,P|_{\Delta^v \le x}$ represents the probability of void cells whose shape factor falls within $x - d\Delta^v/2 \le \Delta^v = \left(\sqrt{Z_1/Z_2}-1\right)/\left(\sqrt{Z_1/Z_2}+1\right) \le x + d\Delta^v/2$. Fig. 8(a) plots the probability density function at the initial state while Fig. 8(b) plots the probability density function after 20% deviatoric strain. It is observed that most void cells are anisotropic with the highest probability around $\Delta^v = 0.2$. For larger friction coefficients, the area fraction occupied by more anisotropic void cells becomes slightly larger while that by less anisotropic void cells becomes slightly smaller.

Figure 8 Probability Density Function $d\,P|_{\Delta^v \le x}/d\Delta^v$ (a) Deviatoric strain 0% (b) Deviatoric strain 20%

The fabric tensor for individual void cell $S_{ij}^{\ v}$ is hence defined such that the major principal fabric as $A^v\left(1+\Delta^v\right)/2$, the minor principal fabric as $A^v\left(1-\Delta^v\right)/2$ and the principal directions are the same as those of $Z_{ij}{}^{v}$. Note that the ratio between the major and minor principal fabrics is $\sqrt{Z_1/Z_2}$.

Anisotropy in void cell orientation

The orientation of void cells can be represented by a unit vector. Similar to contact normal density, the void cell orientations can be characterised by the direction tensor with the form

$$D_{ij}^{S} = d^{S}\begin{pmatrix} \cos\phi^{S} & \sin\phi^{S} \\ \sin\phi^{S} & -\cos\phi^{S} \end{pmatrix} \quad (9)$$

and calculated from its moment tensor, where d^{S} is the anisotropy index and ϕ^{S} the principal direction. The anisotropy index has been plotted in Fig. 9. The principal direction has been all around 90°. The figure suggests that material anisotropy has developed as a result of more void cells orienting towards the loading direction, similar to the observation reported in (Nguyen, Magoariec et al. 2012).

Figure 9 Anisotropy in void cell orientations

Void cell based fabric quantification

The continuum-scale fabric tensor is defined as the average of void cell fabric tensors as:

$$F_{ij}{}^{S} = \frac{1}{N^{v}}\sum_{v\in A} S_{ij}{}^{v} \quad (10)$$

The fabric tensors of individual void cells have been calculated from the void cell geometries obtained from DEM simulations, and used to calculate the macro fabric tensor defined in Eq. (10). The first invariant $F_{ii}{}^{S} = \overline{A^{v}}$ is the average void cell area. The deviatoric part of $F_{ij}{}^{S}$ is an area-weighted measure of void cell shapes. The anisotropy index of void cell-based fabric tensor, Eq.(10), is defined as $d^{F} = 2\left(F^{S}{}_{1} - F^{S}{}_{2}\right)/\left(F^{S}{}_{1} + F^{S}{}_{2}\right)$, where $F^{S}{}_{1}$ and $F^{S}{}_{2}$ are the principal values of the fabric tensor F_{ij}^{S}. The principal direction is observed around 90°. Fig. 10 shows the evolution of the anisotropy index d^{S} during shearing, whose pattern is observed in great similarity as that of contact normal density in Fig. 4(a) and that of void cell orientation in Fig. 9, suggesting a strong correlation among these fabric indices, which will be explored later in this paper.

Figure 10 Anisotropy index of F_{ij}^{S}

Material dilatancy and void cell statistics

Dilatancy is the change in sample volume or void ratio during shearing. For 2D granular assemblies, the total area of assembly A_{sam} is equal to the summation of all void cell areas and can be expressed as:

$$A_{sam} = \sum_{\alpha=1}^{N^{v}} A_{v}^{\alpha} = N^{v}\overline{A^{v}} \tag{11}$$

where A_{v}^{α} denotes the area of the α-th void cell, N^{v} the total number of void cells, and $\overline{A^{v}}$ the average void cell area. The total particle (solid) area $A_{s} = \sum_{\alpha=1}^{N^{p}} A_{p}^{\alpha} = N^{p}\overline{A^{p}}$, where A_{p}^{α} denotes the area of the α-th particle, N^{p} is the total number of particles and $\overline{A^{p}}$ is the average particle area, a constant throughout the test. The void ratio of the granular assembly can hence be formulated as:

$$e = \frac{A_{sam}}{A_{s}} - 1 = \frac{N^{v}}{N^{p}}\frac{\overline{A^{v}}}{\overline{A^{p}}} - 1 \tag{12}$$

The total number of contacts can be found by summing up the coordination numbers of all particles, which however may be slightly different from that summing over all the void cells since in the void cell system each particle-wall contact is counted twice. Should the sample size be large enough, the difference is small and negligible, $M = N^{p}\omega^{p} = N^{v}\omega^{v}$, where the void cell coordination number ω^v denotes the average number of constitutive particles in void cells. It should be no less than 3 in two dimensional granulate systems. The material void ratio can hence be rewritten as:

$$e = \frac{\overline{A^v}}{\overline{A^p}} \frac{\omega^p}{\omega^v} - 1 \tag{13}$$

The volume change tendency, i.e., the dilatancy of granular material, can be quantified as the change in the sample void ratio upon shearing, and studied by tracing the evolution of void cell statistics, in particular $\overline{A^v} \big/ \overline{A^p}$ and ω^v / ω^p during shearing.

Fig. 11(a) plots the particle coordination number ω^p and the void cell coordination number ω^v for pre-sheared samples with different particle friction coefficients. Fig. 11(b) provides information of $\overline{A^v} \big/ \overline{A}^p$ and ω^v / ω^p at various friction coefficients. The data of $\mu_p = 10.0$ are close to those of $\mu_p = 1.0$, and not shown in the figures. Note that the stability condition of two dimensional infinite granulate system imposes the requirement of the minimal coordination number being 3. The coordination numbers slightly smaller than 3 have been observed in this study is partially because non-load bearing particles (rattlers) are present in the system, but not excluded in particle coordination number. It is also because of the boundary effect. At each boundary-particle contact point, there are two force components contributing to the system stability. They are counted twice in void cell construction, but only once when calculating the particle coordination number. For the same reasons, the relationship between the particle coordination number ω^p and the void cell coordination number ω^v is found to slightly deviate from the Euler's relation for planer graphs $\omega^v = 2\omega^p \big/ \left(\omega^p - 2\right)$ (Satake 1985).

Figure 11 The internal structure at initial states (a) Coordination number; (b) Void cell characteristics

The figures show clearly that the particle friction coefficient has a significant effect on void cell characteristics. For frictionless particles, the particle coordination number is only slightly larger than that of void cells. The average void cell area and the average particle area are close. When the particles become frictional, the particle coordination number reduces while the void cell coordination number increases. More frictional particles tend to form fewer but larger void cells. It is observed that with increasing friction coefficients, the number of void cells drops, accompanied with an increase in void cell area. As a result, the average void cell area almost doubles when the particle friction changes from μ_p=0 to μ_p=10. The increase in void cell area exceeds the reduction in void cell number, resulting in larger void ratios observed at higher friction coefficients.

The evolutions of the sample void ratio e and the void cell characteristics, including $\overline{A^v}/\overline{A}^p$, the particle coordination number ω^p and the void cell coordination number ω^v, have been plotted in Fig. 12. Eq. (13) reveals that the change in the void ratio e is resulted from the competition between $\overline{A^v}/\overline{A}^p$ and ω^v/ω^p. As seen in Fig. 12, when samples are sheared, the increase in void cell coordination number is observed and accompanied by an increase in the mean void cell area. When the increase in $\overline{A^v}/\overline{A}^p$ exceeds that in ω^v/ω^p, the sample dilates with an increase in void ratio. Otherwise, the sample contracts with a reduced void ratio.

With zero and low particle frictions, the particle and void cell coordination numbers remain almost constant during shearing. However, for highly frictional particles, shearing causes significant reduction in particle coordination number and increase in void cell coordination number at the early stage of shearing, but this effect is overtaken by the increase in $\overline{A^v}/\overline{A}^p$. Samples show significant dilative responses. These changes during shearing are associated with the development of void cell anisotropies presented in Figs. 8, 9 & 10.

Figure 12 Evolution of void cell statistics to shearing (a) Void ratio e, (b) $\overline{A^v}/\overline{A}^p$, (c) Particle coordination number ω^p and (d) Void cell coordination number ω^v

The void cell coordination number

Frictional particles tend to form larger void cells with higher coordination number. Grouping the void cells according to their coordination number, the total sample area can be expressed as:

$$A_{sam} = \sum_{i=3} H\big|_{val=i} \overline{A^v}\Big|_{val=i} = N^v \sum_{i=3} h\big|_{val=i} \overline{A^v}\Big|_{val=i} \tag{14}$$

where $H_{val=i}$ is the number of void cells whose coordination number is i, $h\big|_{val=i} = H_{val=i}/N^v$ represents its probability and $\overline{A^v}\Big|_{val=i}$ the average area of such void cells. The sample void hence becomes:

$$e = \frac{A_{sam}}{A_s} - 1 = \frac{N^v}{N^p} \sum_{i=3} \left(h\big|_{val=i} \overline{A^v}\Big|_{val=i} \Big/ \overline{A}^p \right) - 1 \tag{15}$$

where N^v stands for the total number of void cells.

Fig. 13 gives the probability and the average area of void cells with different coordination numbers at the initial and sheared states. It shows clearly that there is a close correlation between the average void cell area and the coordination number. The correlation can be roughly approximated by the polynomial function of power 2, and is found independent of particle friction coefficients. Particles with higher friction coefficients are more likely to form void cells with more constitutive particles, hence the probability of void cells with a larger coordination number is higher. Shearing alters the correlation between $\overline{A^v}/\overline{A}^p$ and the cell coordination number ω^v slightly. Data at 20% deviatoric strain are shown in Fig. 13(b). At the same coordination number, $\overline{A^v}/\overline{A}^p$ is smaller at the sheared states than that in the initial state, indicating the dependence of average void cell area on void cell anisotropy.

Figure 13 Void cell statistics at different coordination number (μ_p =0.5) (a) Deviatoric strain 0%; (b) Deviatoric strain 20%.

VOID VECTOR BASED FABRIC QUANTIFICATION AND MATERIAL STRAIN

Using the void cell system, the strain of a granular assembly can be considered as the volume weighted average of void cell strains. The micro-structural strain definition expresses the continuum-scale material strain in terms of particle relative displacements and void vectors (Bagi 1996, Kruyt and Rothenburg 1996, Kuhn 1999, Li, Yu et al. 2009), and inspired the definition of void vector fabric tensors.

The micro-structural strain tensor

Following the sign convention defined in (Li, Yu et al. 2009), the compressive strain is positive. $\mathbf{n}(\mathbf{x})$ denotes the normal direction on the boundary surface at point $\mathbf{x}$, positive when pointing inwards. In two dimensional spaces, the displacement gradient tensor averaged over the sample area A could be evaluated as:

$$\bar{e}_{ij} = -\frac{1}{A}\oint_A u_{j,i}\mathrm{d}A = \frac{1}{A}\oint_B \mathbf{u}\otimes\mathbf{n}dL \qquad (16)$$

where $u_{j,i}$ denotes the displacement gradient and L is the boundary of the area of interest A. The line integral on the right hand side follows the counter-clockwise integration paths over the boundary of the area A. With ϕ_{ij} represents the two dimensional permutation tensor $\phi_{ij} = \begin{pmatrix} 0 & 1 \\ -1 & 0 \end{pmatrix}$, $n_i dL = \phi_{ij} dx_j$. Eq. (16) becomes:

$$\bar{e}_{ij} = \frac{\phi_{jk}}{A} \oint_B u_i dx_k = -\frac{\phi_{jk}}{A} \oint_B x_k du_i \tag{17}$$

With the material internal structure represented by the void cell system, Eq. (17) can be discretized into:

$$\bar{e}_{ij} = -\frac{\phi_{jk}}{A} \sum_{v \in A} \sum_{L^v} x_k \Delta u_i = -\frac{\phi_{jk}}{A} \sum_{v \in A} \sum_{L^v} \upsilon_k \Delta u_i \tag{18}$$

where υ_i is the vector starting from the contact point to the void cell centre, referred to as the void vector. Eq. (18) is a double summation. The inner summation $\sum_{L^v} *$ runs over the boundary L^v of void cell v and $\sum_{v \in A} *$ is a summation over all the void cells within the sample area A. For granular materials, no matter how the sample is divided into sub-domains; the weighted sum of local displacement gradient tensors is always the same (Bagi 1993). Denoting

$$e_{ij}{}^{v} = -\frac{\phi_{jk}}{A^v} \sum_{L^v} \upsilon_k \Delta u_i \tag{19}$$

as the local displacement gradient tensor defined on the void cell v, the sample displacement gradient tensor can be written as the area-weighted average over all the void cells:

$$\bar{e}_{ij} = \frac{1}{A} \sum_{v \in A} \left(A^v e_{ij}{}^{v} \right) \tag{20}$$

It is verified that such estimated sample displacement gradient is in good agreement with the value obtained from sample boundary.

Void vector based fabric quantification

The micro-structural strain definition given in Eq. (18) shows that the key geometrical information bridging-up the continuum scale strain and the particle-scale relative displacements is void vector, which connects the contact point to the void cell centre. This inspired the void vector based fabric tensor definitions (Li and Li 2009). The mathematical treatment has been detailed in (Li and Yu 2011) and applied to analyze the contact vectors in the previous session.

Fabric quantification based on void vector probability density

To describe the directional dependence of void vectors, it is of interest to know in each direction 1) their probability density and 2) their representative (or mean) value. The directional probability density of void vectors can be quantified in terms of a second rank deviatoric tensor

$$D_{ij}^{v} = d^{v} \begin{pmatrix} \cos\phi^{v} & \sin\phi^{v} \\ \sin\phi^{v} & -\cos\phi^{v} \end{pmatrix} \tag{21}$$

following the similar procedure to process information on contact normal and void cell orientations.

Fabric quantification based on void vector length

As a description of void cell shape in average, the directional dependence of mean void vector has been characterized in terms of the second rank deviatoric tensor $G_{ij}^{v} = B^{v} \begin{pmatrix} \cos\beta^{v} & \sin\beta^{v} \\ \sin\beta^{v} & -\cos\beta^{v} \end{pmatrix}$ so that the mean void vector in direction $\mathbf{n}$ can be approximated as

$$\upsilon(\mathbf{n}) = \upsilon_0 \left[1 + B^{v} \cos\left(2\theta - \beta^{v}\right) \right] \tag{22}$$

where in two dimensional spaces, the unit direction vector is equivalently expressed as $\mathbf{n} = \left(\cos\theta, \sin\theta\right)$. Based on the mean void vector length, (Li and Li 2009) proposed the void vector based fabric tensor as:

$$H_{ij}{}^{v} = \upsilon_0 \left(\delta_{ij} + G_{ij}^{v} \right) \tag{23}$$

The void vector based moment tensor

The void vector based moment tensor can be considered as a combined account of the anisotropies in void vector density and mean void vector length. It has been used in (Fu and Dafalias 2015) in structural characterization. The moment tensor can be found as

$L_{ij}^{v} = \left\langle \upsilon_i n_j \right\rangle = \frac{1}{M}\sum_{\alpha=1}^{M} \upsilon_i^{\alpha} n_j^{\alpha}$. Similar to previous discussions on contact vectors, L_{ij}^{v} can be determined from D_{ij}^{v} and H_{ij}^{v}. In two dimensional spaces, $L_{ij}^{v} = \upsilon_0 \left[\frac{1}{2}\left(\delta_{ij} + G_{ij}^{v}\right) + \frac{1}{4}\left(D_{ij}^{v} + D_{im_1}^{v} G_{jm_1}^{v}\right) \right]$.

Internal structure size during shearing

As shearing continues, anisotropy in void vectors develops and is quantified with the two anisotropy indices d^{v}, B^{v}. Both anisotropies are observed to be significant. For all the simulations in this study, both anisotropies align in the loading direction. And similarity is observed between their evolutions and those in contact normal density and void cell orientation. The directional average of void vector length υ_0 is regarded as a measure of the void cell size, and plotted in Fig. 14. It is shown that samples with larger particle friction coefficients have a larger void vector length, corresponding to larger void cells.

Figure 14 Directional average of void vector length

CORRELATION BETWEEN DIFFERENT FABRIC QUANTIFICATIONS

So far, a number of fabric quantifications have been listed in this paper and defined as the statistical characterisatics of contacts, void cells and void vectors, respectively. They are chosen because of their relevance to material strength and deformation, and formulated based on the directional statistical theory (Kanatani 1984, Li and Yu 2011). The development of constitutive model however requires minimizing the number of variable and parameters. It is hence important to explore the correlations among various fabric quantifications (Fu and Dafalias 2015). The similarities observed in their evolution pattern is encouraging. In this session, the void cell based fabric tensor F_{ij}^{S} has been used as a reference to discuss the correlaton among different fabric quantifications.

Among all the fabric tensors, two of them contains informaton reflecting void cell size. They are the fabric tensor based on void vector length H_{ij}^{v}, Eq. (23) and the void cell based fabric tensor F_{ij}^{S}, Eq. (10). The directional averaged void vector length υ_0 in H_{ij}^{V} and the mean void cell area $F_{ii}^{S} = \overline{A^v}$ in F_{ij}^{S} are plotted against each other in Fig. 15, showing a strong correlation in between. It confirms that υ_0 can be considered as an effective descriptor of material internal structure size. The correlation is independnt of particle friction coefficient.

Figure 15 Correlations between internal structure size descriptors

All the fabric tensors contains material anisotropy information. The anisotropy developed in contact vector length G_{ji}^{c} is not elaborated here because its effect is secondary. The anisotropy index d^F in the void cell based fabric quantification F_{ij}^{S}, Eq. (10) is shown correlated with other anisotropy indices, including d^c in contact normal density, Eq. (3), d^S in void cell orientation, Eq. (9), d^v in the void vector orientation, Eq. (21) and B^v in the mean void vector length, Eq. (23) in Fig. 16. The strong correlation among these anisotropy confirms the observations made in (Li, Yu et al. 2009, Fu and Dafalias 2015). The anisotropy indices associated with void vectors are expected to be closely related that in void cells, as confirmed in Fig. 16(c) & (d). In-depth investigation into structural topology may help to establish the correlation analytically and to unify the fabric tensor definitions.

Figure 16 Correlations between the void cell-based anisotropy and other anisotropy indices

(a) Contact normal probability density; (b) Void cell orientation; (c) Void vector probability density and (d) Mean void vector length

DISCUSSION ON STRAIN HETEROGENITY

Observation of deformation pattern

Strain heterogeneity is another important feature of granular materials. The deformation descriptor in Eq. (19) is defined for each individual void cell and offers a view of spatial distribution of material deformation. Take the configuration when the void cell system is constructed as the reference undeformed configuration. The relative displacements occurring during the subsequent 0.5% deviatoric strain increments are extracted from the DEM simulations and used to calculate the displacement gradient tensor of each void cell as per Eq. (19).

Fig. 17 shows the local displacement gradients of each void cell when the sample was sheared from 15% to 15.5% deviatoric strain. The four components of non-affine displacement gradient tensor, defined as the deviation of the local strain from the sample average displacement gradient tensor, for the sample with $\mu_g = 0.5$ are plotted in the separate sub-figures. It is observed that there are localized banding structures where the strain is much more significant than the remaining of areas. This is similar to the observation made in (Kuhn 1999) that slip deformation was most intense within thin obliquely micro bands. Different from the periodic boundaries used in (Kuhn 1999), the sample boundaries are rigid walls which impose uniform displacement gradient field. These banding structures do not persist during shearing. Subsequent loading continuously destroys the existing banding structures and promotes the formation of new bands in other locations. It is interesting to note that although certain banding features are commonly observed in the four plots; the patterns for the two shear strain components are observed to be different from those for the two normal strain components.

Furthermore, bands of component ${e_{12}}^{w}$ tend to propagate in the vertical direction while the pattern shown by component ${e_{21}}^{w}$ extends in the horizontal direction.

Figure 17 Patterns of non-affined deformation gradient observed from deviatoric strain $\varepsilon_q = 15\%$ to $\varepsilon_q = 15.5\%$ ($\mu_g = 0.5$) (a) ε_{11} (b) ε_{12} (c) ε_{21} and (d) ε_{22}

The distance between deformation bands is in the order of tens of particle diameters. It is several times larger than the internal scale in force chain heterogeneity. Shearing brings about continuous formation, development and dissolution of deformation bands, causing synchronized swing in the material shear stresses as seen in Fig. 2(a). The developments of the force chain heterogeneity and the deformation bands are believed to be critical to the deformation and failure of granular systems. It is an area of future research. Considering the heterogeneity in material deformation, the sample size may need to be further enlarged to serve as a representative element.

Probability distributions

The sample deformation gradient tensor given in Eq. (20) can be interpreted as an integral over all the possible local deformation gradient values as

$$\bar{e}_{ij} = \int W\big|_{e_{ij}} e_{ij} de_{ij} \tag{24}$$

in which $W\big|_{e_{ij}} = \dfrac{1}{A} \lim\limits_{\Delta e_{ij} \to 0} \dfrac{\sum A^v\big|_{e_{ij}^v \in \left(e_{ij} - \Delta e_{ij}/2, e_{ij} + \Delta e_{ij}/2\right)}}{\Delta e_{ij}}$ is the area fraction density function. It is the area fraction of void cells whose displacement gradient component ${e_{ij}}^{v}$ falls within the range $e_{ij}^{v} \in \left(e_{ij} - \Delta e_{ij}/2, e_{ij} + \Delta e_{ij}/2\right)$ normalized by the deformation increment Δe_{ij}. Eq. (24) deals with the four components of displacement gradient tensor separately. The Einstein summation over the repeated subscripts doesn't apply here.

Figure 18 Area fraction density of the four displacement gradient components ($\mu_g = 0.5$, from $\varepsilon_q = 15\%$ to $\varepsilon_q = 15.5\%$) (a) normal components and (b) shear components

Fig. 18 plots the area fraction density function for the four components of displacement gradient tensor. The data are again taken from the sample with $\mu_g = 0.5$ when sheared from $\varepsilon_q = 15\%$ to $\varepsilon_q = 15.5\%$ as shown in Fig. 17. For all the simulations in this study, the highest area fraction occurs at zero or near zero deformation. The area fraction decreases quickly as the magnitude of strain component increases. However, it is worth noting that there exists a large area fraction where local deformation is much more prominent than the continuum scale average 0.5%. Although the samples are loaded in the biaxial mode, significant shear strains are observed, indicating rigid body rotation or deformation deviated away from the vertical direction are important deformation mechanisms in local void cells. The continuum-scale deformation is of small magnitudes because there are significant portions of positive as well as negative strain components which compensate each other.

Particle friction coefficient has a significant influence on deformation distribution. Samples of smooth particles show more dispersed but more significant void cell deformations. Fig. 19 presents the probability distribution of void cell deformations by plotting the area fraction of positive and negative normal strains and the averages of positive and negative shear strain components respectively. The shape of function $W\big|_{e_{ij}}$ for the two shear components is symmetric with respect to $x = 0$, corresponding to the observation that the area fractions for the positive and negative shear components are around 50%, although not plotted here.

Figure 19 Development of void cell strains (a) $\mu_p = 0.0$ (b) $\mu_p = 0.5$ and (c) $\mu_p = 10.0$

With increase in particle friction coefficient, the area fraction with positive e_{22} and negative e_{11} increase as shown in Fig. 19. For frictionless particles $\mu_g = 0.0$, there are extensive and significant deformations observed in all void cells. Around 55% of sample area goes through positive e_{22} or negative e_{11} which is only slightly larger than the area fraction 45% for negative e_{22} or positive e_{11}. The average magnitudes of normal strain components are around 2%, and of shear strain components around 4%. However, with larger particle friction coefficient, for example, in the case $\mu_g = 0.5$, there is nearly 70% percent of area with positive e_{22} or negative e_{11}. The average magnitudes of normal strain components are around 1% with a slightly larger value for shear strain components. The average magnitudes are observed to increase slightly at the extremely high particle friction coefficient $\mu_g = 10.0$ indicating the deformation distribution gets slightly dispersed. Differences have also been observed in deformation at small strain levels. For higher particle friction coefficients, the local void cell deformation is more uniform and close to the continuum-scale average deformation, i.e., smaller non-affine deformation. And it takes a larger strain level to develop into the deformation patterns at the critical states.

There is however not yet a clear conclusion on what fabric information affects strain heterogeneity and the consequent impact on material deformation. The relative displacement between particles may result from different combinations of contact sliding and rolling (Iwashita and Oda 1998, Kuhn and Bagi 2004). More research in studying local particle rearrangement and contact movement (Nguyen, Magoariec et al. 2012) is needed.

CONCLUDING REMARKS

This paper studies the behavior of granular material as the collective response of void cells based on the multi-scale data obtained from a series of numerical simulations with different particle friction coefficients. More anisotropic structures have been formed in more frictional materials, and they can support larger contact force anisotropies. The difference in particle friction coefficient also causes significant difference in internal structure size. More frictional particles tend to form less but larger void cells, leading to a larger sample void ratio.

The definition of fabric tensor requires 1) identifying the key aspect of material internal structure and 2) understanding its influence on the stress-strain responses. Three groups of fabric tensor have been covered in this paper. The first one is based on contact vectors. Fabric tensors based on contact normal density and the contact vector moment tensors are identified as effective indices associated with material strength, and their impact on material stress quantified by the SFF relationship. The second group is defined on void cell characteristics. The fabric tensor based on the area moment of inertia S_{ij}^{v} has been proposed to characterize the individual void cell geometry and their statistical average as material fabric tensor, Eq. (10). Fabric tensors have been defined based on the void cell orientation and as the statistical average of void cell characteristics. Material dilatancy can be interpreted by tracing the void cell statistics during shearing. For frictionless particles, shearing doesn't change the void cell size much. However, for high friction particles, shearing will form larger void cells, causing dilative material responses. The micro-structural strain definition given in Eq. (18) suggests the void vector based fabric tensor definitions could be potential candidates when studying material deformation, including those based on void vector probability density and the directional distribution of mean void vectors.

Correlations among various fabric quantifications have been explored. The mean void vector length and the mean void cell area are parameters quantifying the internal structure size, and strongly correlated with each other. Anisotropy indices defined based on contact normal density, void vector density, void vector length and void cell orientation are found effective in characterizing loading-induced anisotropy. They are also closely correlated. The fabric tensor definitions, such as the fabric tensors defined on the void vector length and that based on individual void cell characteristics, are advantageous for reflecting both the internal structure size and material anisotropy. In-depth investigation on structural topology may help establish the correlation among different fabric descriptors and unify the fabric tensor definition.

Deformation of granular materials is highly heterogeneous. The deformation of individual void cells has been calculated and the local deformation is shown to be much more significant than the continuum-scale average strain. Deformation bands have been observed. With sample boundaries formed by rigid planar walls, shearing continuously destroys the existing banding structures and promotes the formation of new bands in other locations. The distance between these deformation bands is in the scale of tens of particle diameters. Its relation to and impact on material deformation is an area of future investigation.

REFERENCES

Antony, S. J. and M. A. Sultan (2007). "Role of interparticle forces and interparticle friction on the bulk friction in charged granular media subjected to shearing." Physical Review E **75**(3).

Bagi, K. (1993). On the definition of stress and strain in granular assemblies through the relation between micro- and macro-level characteristics. Powders & Grains 93. C. Thornton, A.A.Balkema**:** 117-121.

Bagi, K. (1996). "Stress and strain in granular assemblies." Mechanics of Materials **22**: 165-177.

Blumenfeld, R. and S. F. Edwards (2006). "Geometric partition functions of cellular systems: explicit calculation of entropy in two and three dimensions." The European Physical Journal E **19**: 23-30.

Christoffersen, J., Mehrabadi, M.M., Nemat-Nasser, S. (1981). "A micromechanical description of granular material behaviour." Journal of Applied Mechanics, ASME **48**: 339-344.

Cundall, P. A. and O. D. L. Strack (1979). "A discrete numerical model for granular assemblies." Geotechnique **29**(1): 47-65.

Fu, P. and Y. F. Dafalias (2015). "Relationship between void- and contact normal-based fabric tensors for 2D idealized granular materials." International Journal of Solids and Structures **63**: 68-81.

Huang, X., K. J. Hanley, C. O'Sullivan and C. Y. Kwok (2014). "Exploring the influence of interparticle friction on critical state behaviour using DEM." International Journal for Numerical and Analytical Methods in Geomechanics **38**(12): 1276-1297.

Itasca Consulting Group Inc. (1999). PFC2D (Particle Flow Code in Two Dimensions). Minneapolis, ICG.

Iwashita, K. and M. Oda (1998). "Rolling resistance at contacts in simulation of shear band development by DEM." Journal of Engineering Mechanics **124**(3): 285-292.

Kanatani, K.-I. (1984). "Distribution of directional data and fabric tensors." International Journal of Engineering Science **22**(2): 149-164.

Kruyt, N. P. and L. Rothenburg (1996). "Micromechanical definition of the strain tensor for granular materials." Journal of Applied Mechanics **118**: 706-711.

Kruyt, N. P. and L. Rothenburg (2014). "On micromechanical characteristics of the critical state of two-dimensional granular materials." Acta Mechanica **225**: 2301-2318.

Kuhn, M. R. (1999). "Structured deformation in granular materials." Mechanics of Materials **31**(6): 407-429.

Kuhn, M. R. and K. Bagi (2004). "Contact rolling and deformation in granular media." International Journal of Solids and Structures **41**: 5793-5820.

Li, X.-S. and Y. F. Dafalias (2012). "Anisotropic critical state theory: role of fabric." Journal of Engineering Mechanics **2012**: 263-275.

Li, X. and X.-S. Li (2009). "Micro-macro quantification of the internal structure of granular materials." Journal of Engineering Mechanics **135**(7): 641-656.

Li, X. and H.-S. Yu (2011). "Tensorial Characterisation of Directional Data in Micromechanics." International Journal of Solids and Structures **48**(14-15): 2167-2176.

Li, X. and H.-S. Yu (2013). "On the stress-force-fabric relaitonship for granular materials." International Journal of Solids and Structures **50**(9): 1285-1302.

Li, X. and H.-S. Yu (2014). "Fabric, force and strength anisotropies in granular materials: a micromechanical insight." Acta Mechanica **225**(8): 2345-2362.

Li, X., H.-S. Yu and X.-S. Li (2009). "Macro-micro relations in granular mechanics." International Journal of Solids and Structures **46**(25-26): 4331-4341.

Li, X., H.-S. Yu and X.-S. Li (2013). "A virtual experiment technique on the elementary behaviour of granular materials with DEM." International Journal for Numerical and Analytical Methods in Geomechanics **37**(1): 75-96.

Nguyen, N.-S., H. Magoariec and B. Cambou (2012). "Local stress analysis in granular materials at a mesoscale." International Journal for Numerical and

Analytical Methods in Geomechanics **36**: 1609-1635.

Nguyen, N. S., H. Magoariec, B. Cambou and A. Danescu (2009). "Analysis of structure and strain at the meso-scale in 2D granular materials." International Journal of Solids and Structures **46**: 3257-3271.

Oda, M., S. Nemat-Nasser and J. Konishi (1985). "Stress-induced anisotropy in granular masses." Soils and Foundations **25**(3): 85-97.

Oda, M., Nemat-Nasser, S. and Konishi, J. (1985). "Stress-induced anisotropy in granular masses." Soils and Foundations **25**(3): 85-97.

Peyneau, P.-E. and J.-N. Roux (2008). "Frictionless bead packs have macroscopic friction, but no dilatancy." Physical Review E **78**: 011307.

Rothenburg, L. and R. J. Bathurst (1989). "Analytical study of induced anisotropy in idealised granular material." Ge´otechnique **39**(4): 601-614.

Rothenburg, L. and A. P. S. Selvadurai (1981). A micromechanical definition of the Cauchy stress tensor for particulate media. Proceedings of the International Symposium on Mechanical Behaviour of Structured Media. A. P. S. Selvadurai. Ottawa, Canada**:** 469-486.

Satake, M. (1978). Constitution of mechanics of granular materials through graph representation. U.S.-Japan Seminar on Continuum-Mechanical and Statistical Approaches in the Mechanics of Granular Materials. S. C. Cowin and M. Satake. Gakujutsu Bunken Fukyukai, Tokyo**:** 47-62.

Satake, M. (1982). Fabric tensor in granular materials. Deformation and Failure of Granular materials. V. a. Luger, Balkema**:** 63-68.

Satake, M. (1983). Fundamental quantities in the graph approach to granular materials. Mechanics of Cohesive-Frictional Materials: New Models and Constitutive Relations. J. T. Jenkins and M. Satake**:** 9-19.

Satake, M. (1985). Graph-theoretical approach to the mechanics of granular materials. 5th International Symposium on Continuum Models of Discrete Systems. Nottingham**:** 163-173.

Skinner, A. E. (1969). "A note on the influence of interparticle friction on the shearing strength of a random assembly of spherical particles." Geotechnique **19**(1): 150-157.

Thornton, C. (2000). "Numerical simulation of deviatoric shear deformation of granular media." Geotechnique **50**(1): 43-53.

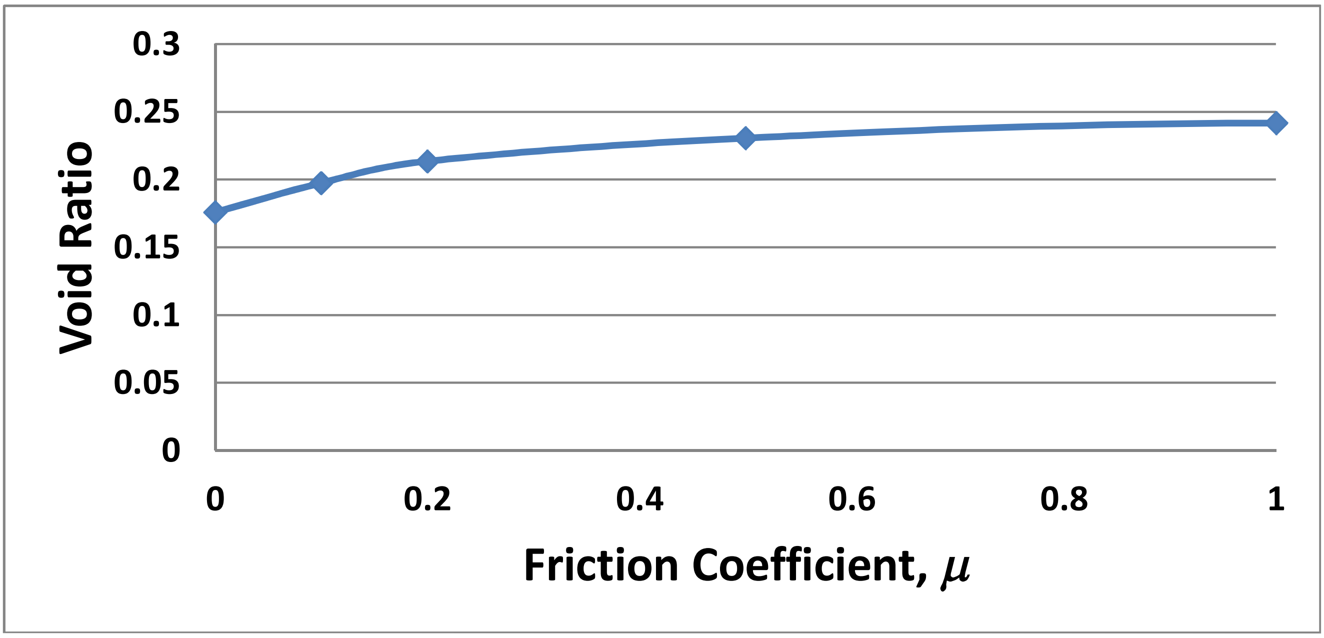
0.3
0.25
0.2
0.15
0.1
0.05
0
Void Ratio
0
0.2
0.4
0.6
0.8
1
Friction Coefficient, μ

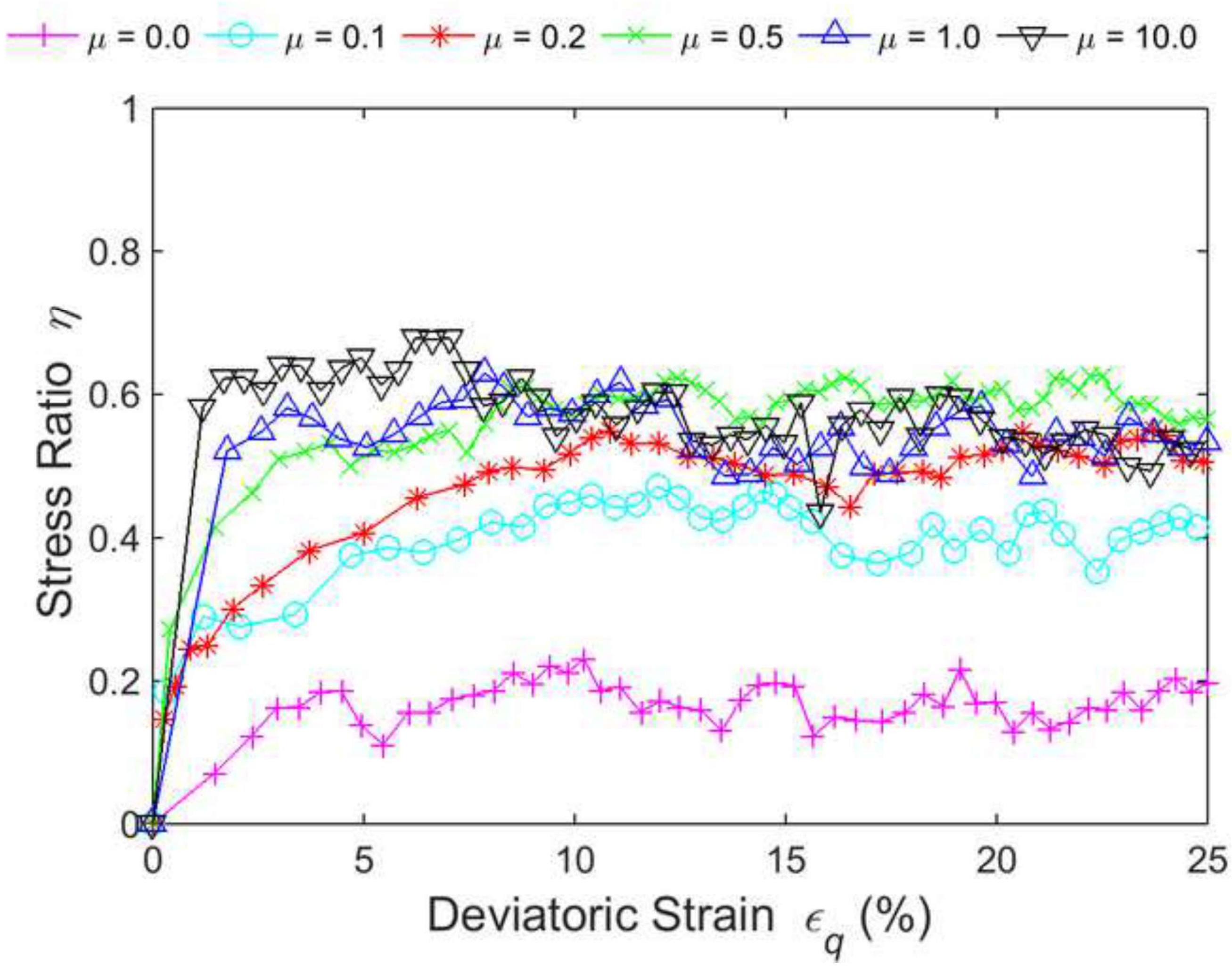

μ = 0.0
μ = 0.1
μ = 0.2
μ = 0.5
μ = 1.0
μ = 10.0
Stress Ratio η
Deviatoric Strain ϵq (%)
0
0.2
0.4
0.6
0.8
1
0
5
10
15
20
25

Figure

Click here to download Figure Fig-2b.tif

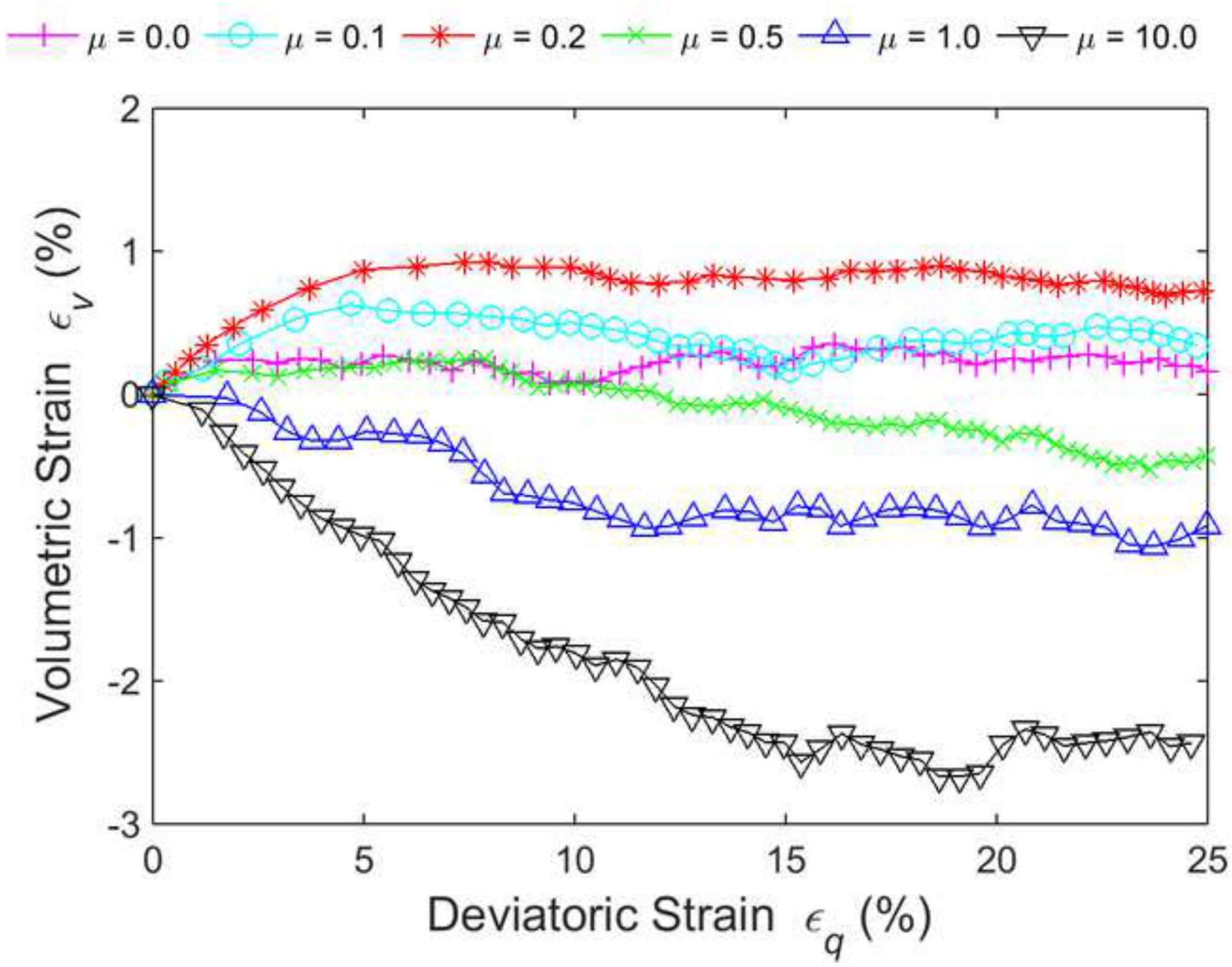

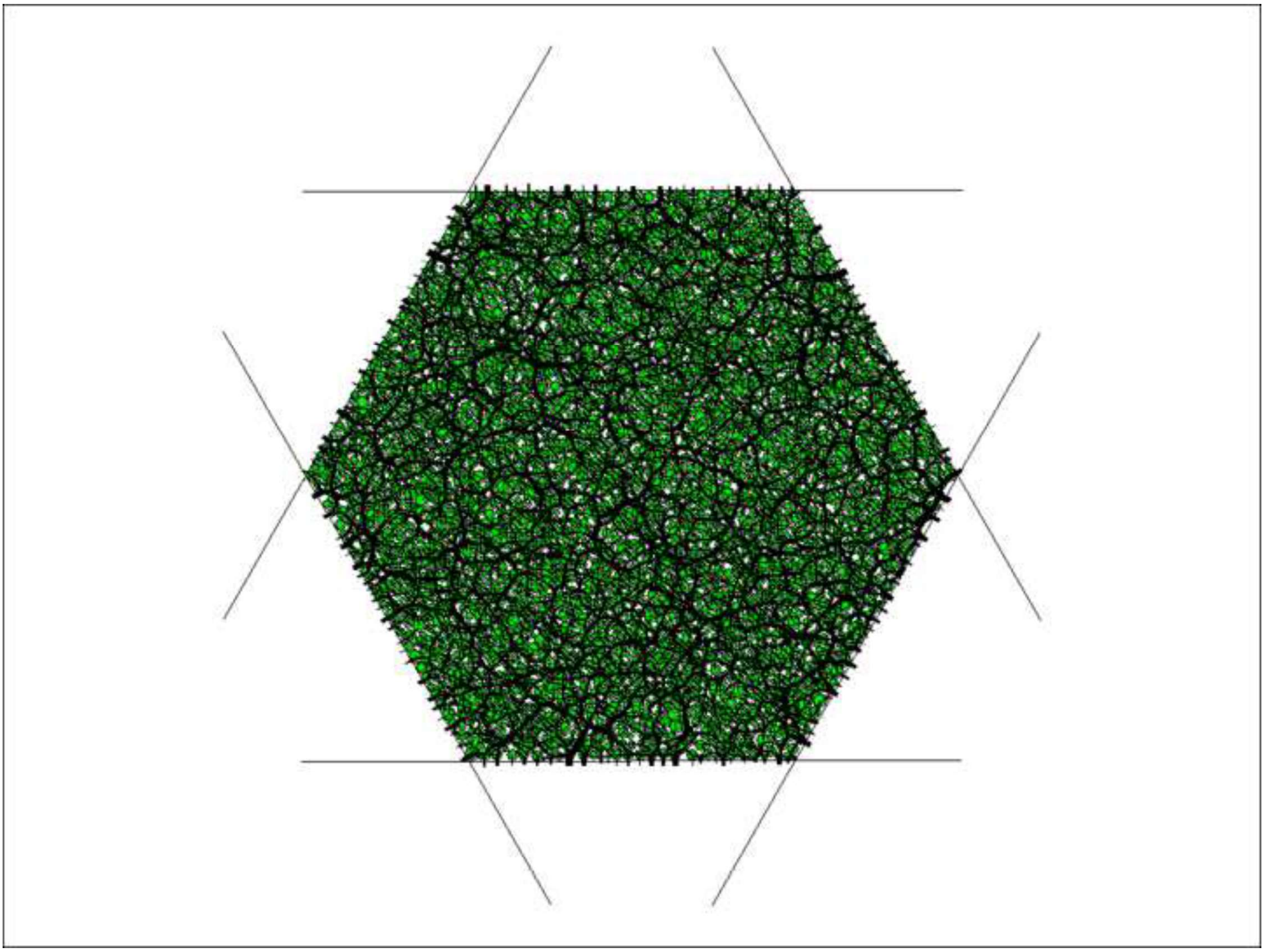

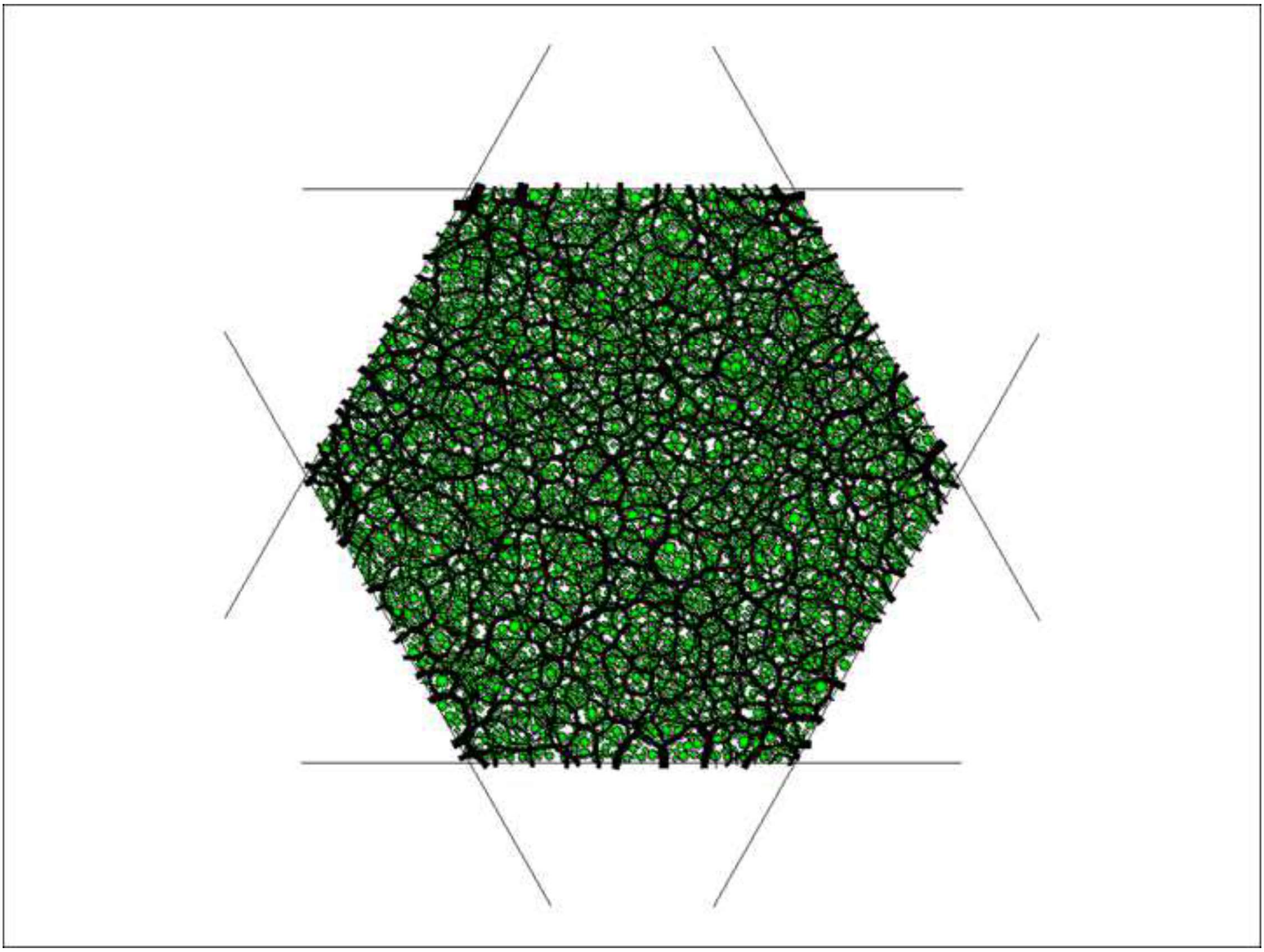

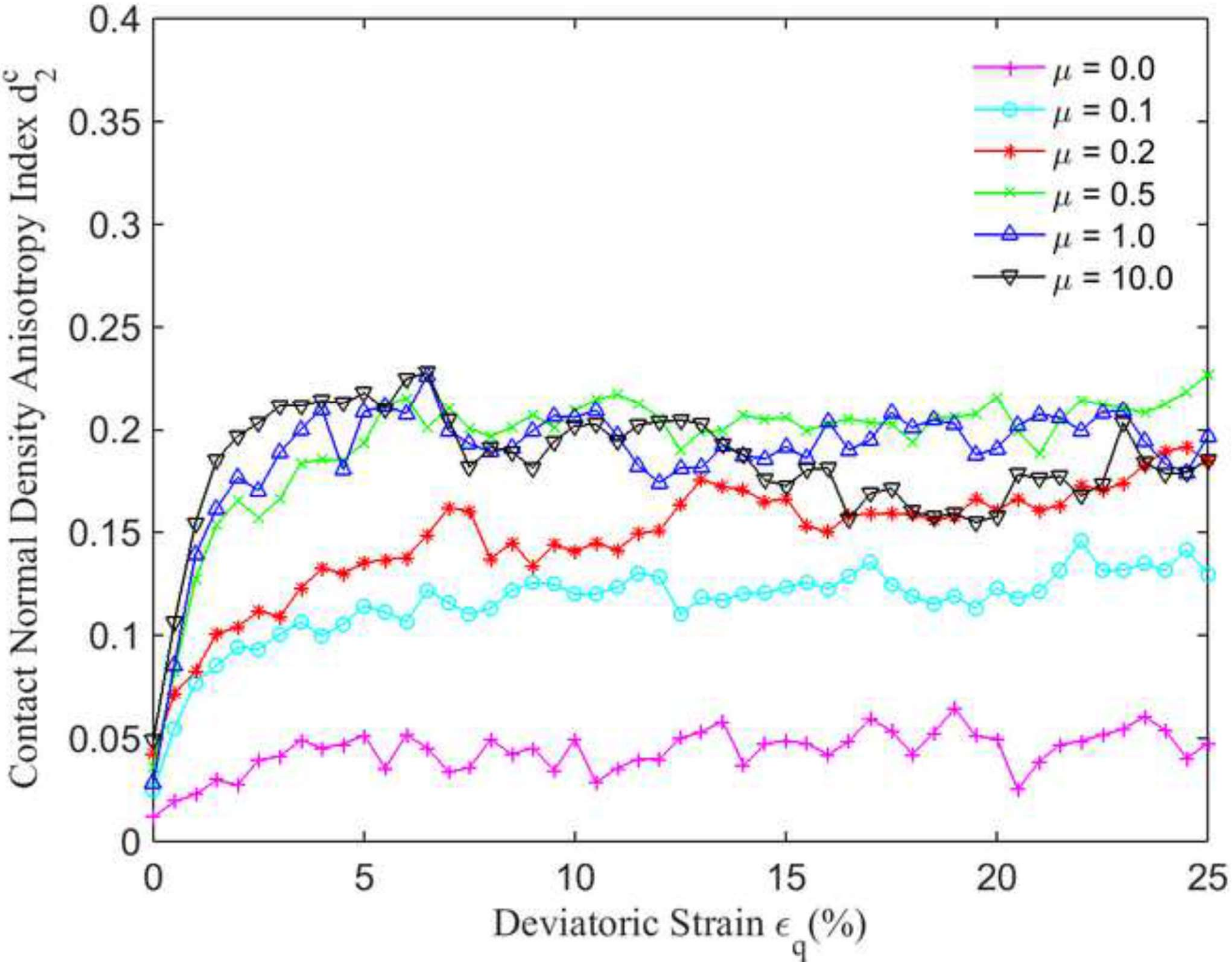
Contact Normal Density Anisotropy Index d_2^c
Deviatoric Strain ϵ_q (%)
μ = 0.0
μ = 0.1
μ = 0.2
μ = 0.5
μ = 1.0
μ = 10.0
0.4
0.35
0.3
0.25
0.2
0.15
0.1
0.05
0
0
5
10
15
20
25

Click here to download Figure Fig-4b.tif

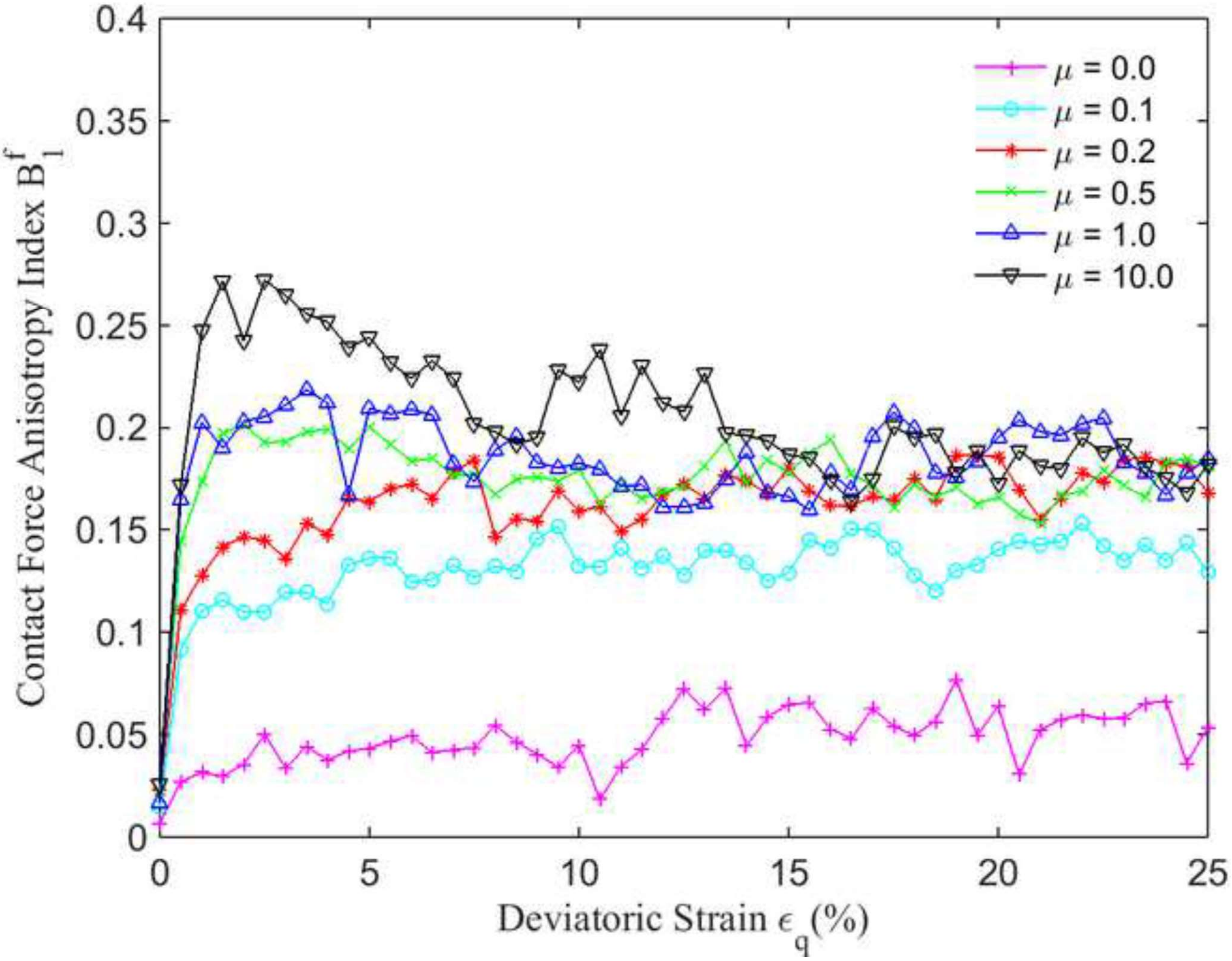

Click here to download Figure Fig-5.tif

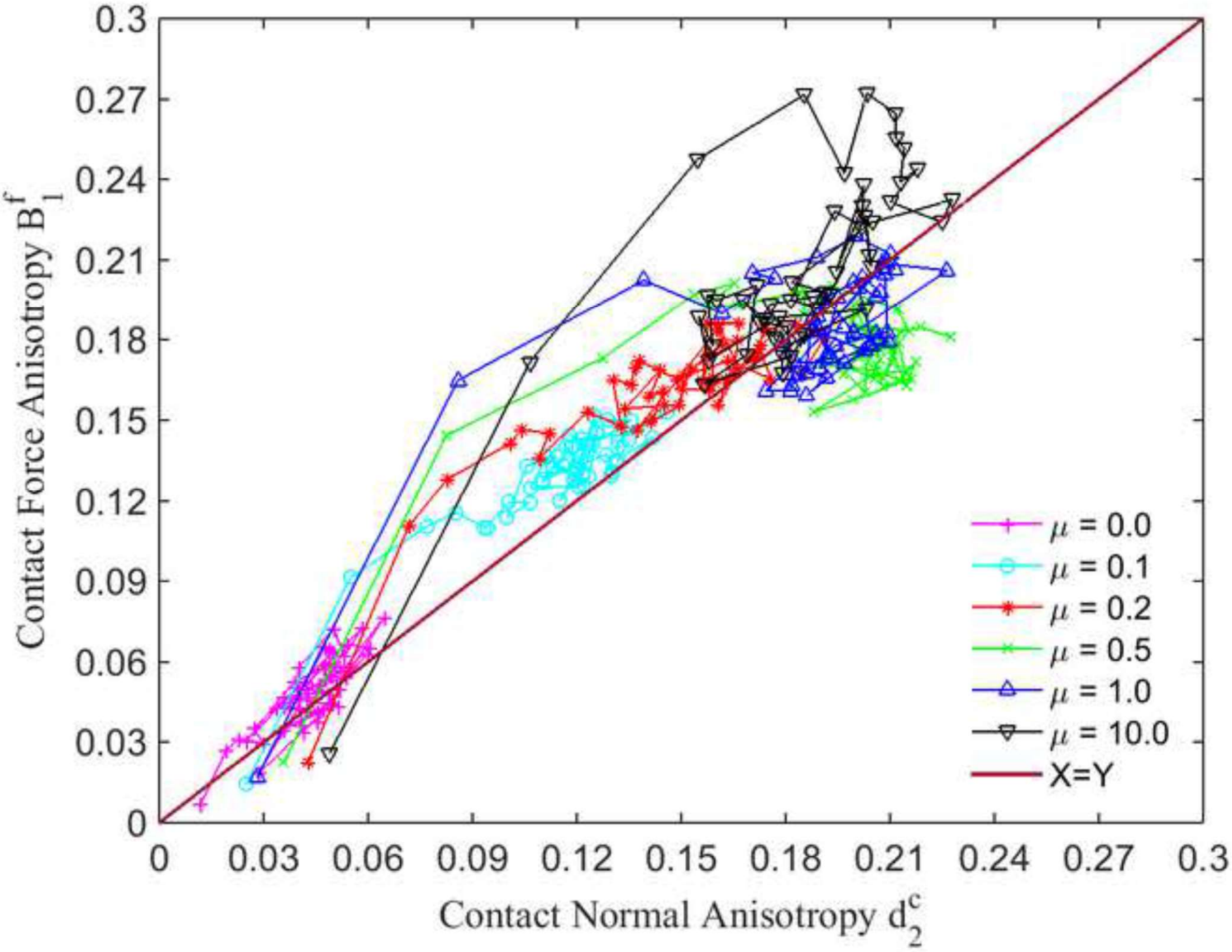

Figure

Click here to download Figure Fig-6.pdf

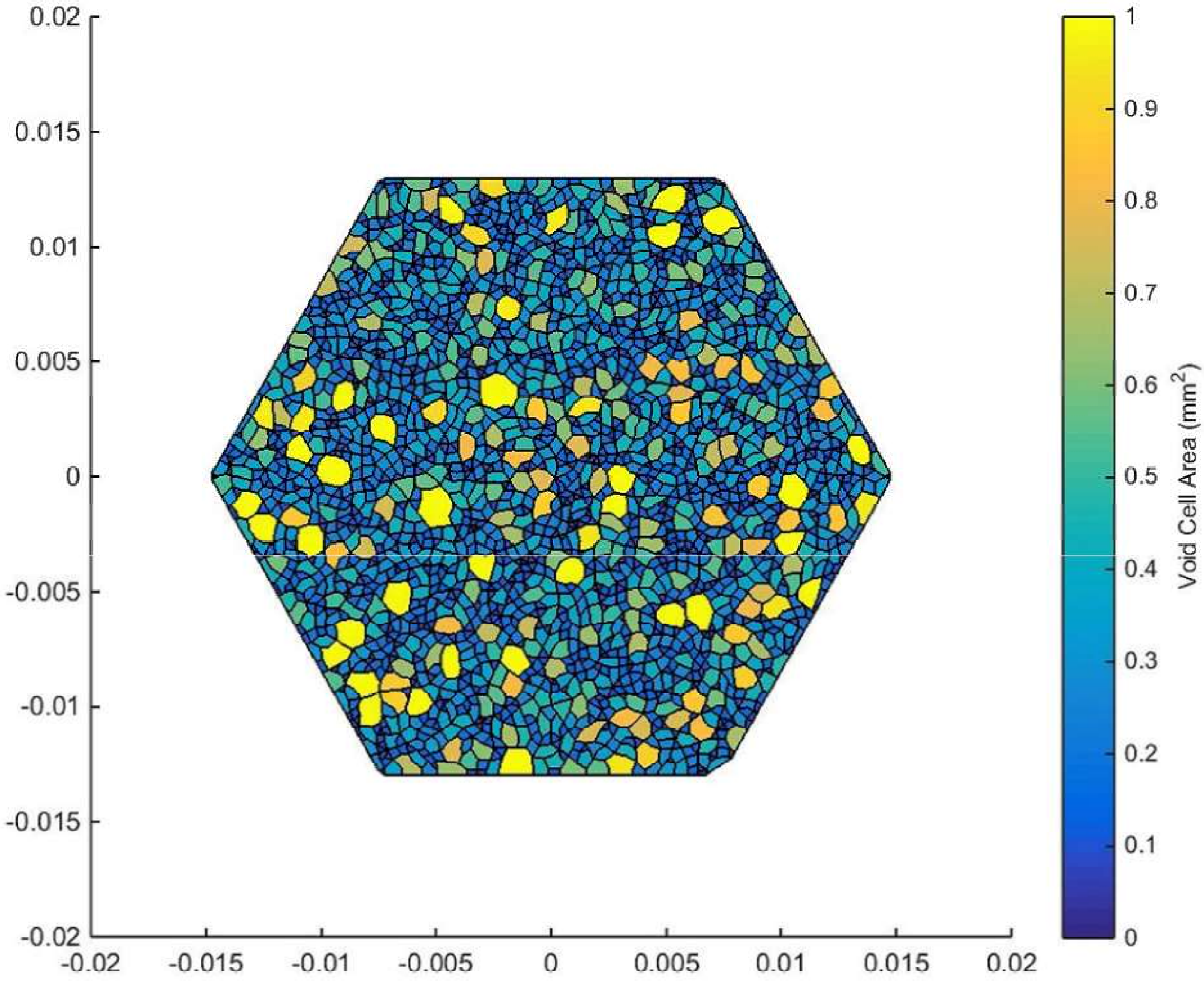

Figure

Click here to download Figure Fig-7.pdf

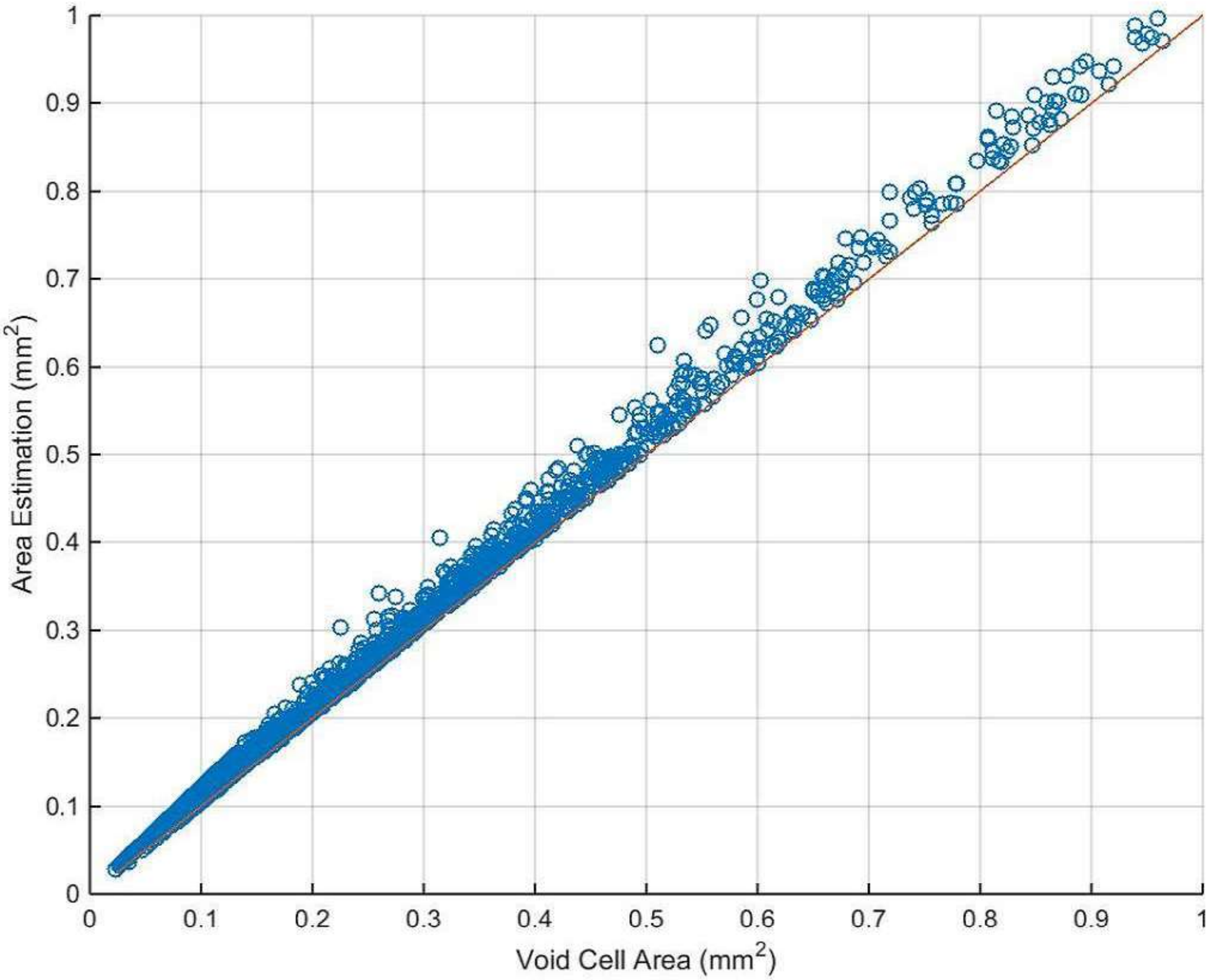

Click here to download Figure Fig-8a.tif

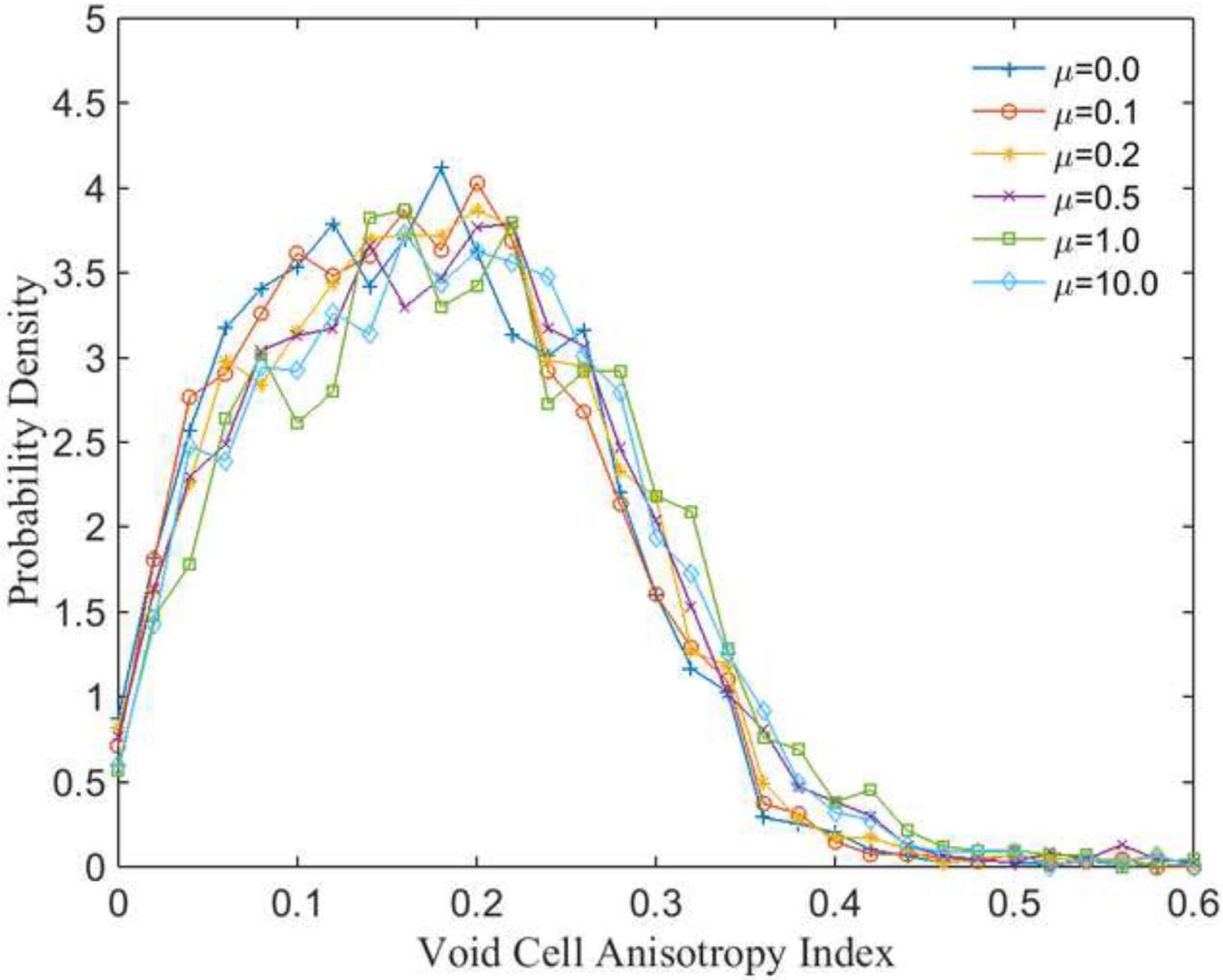

Click here to download Figure Fig-8b.tif

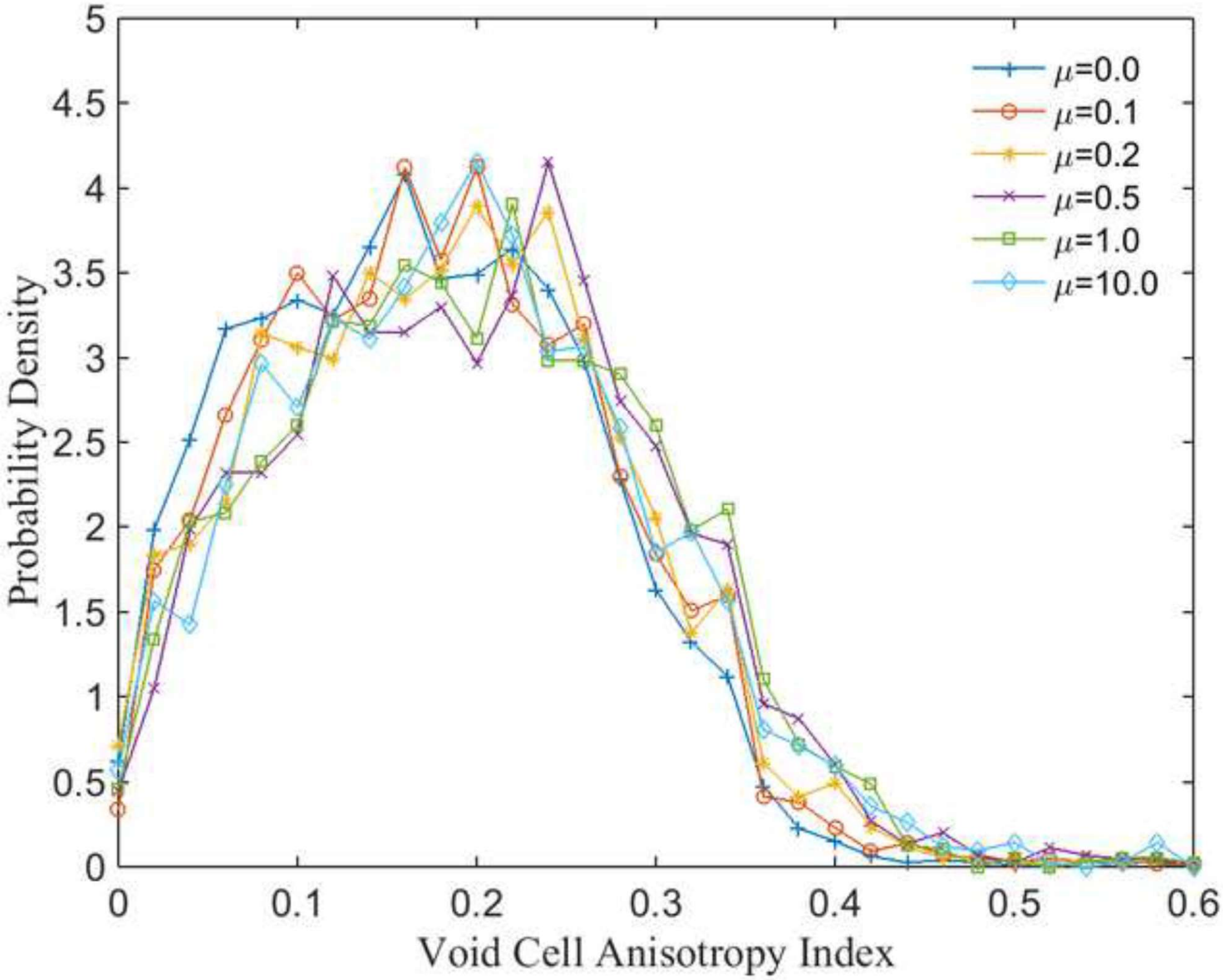

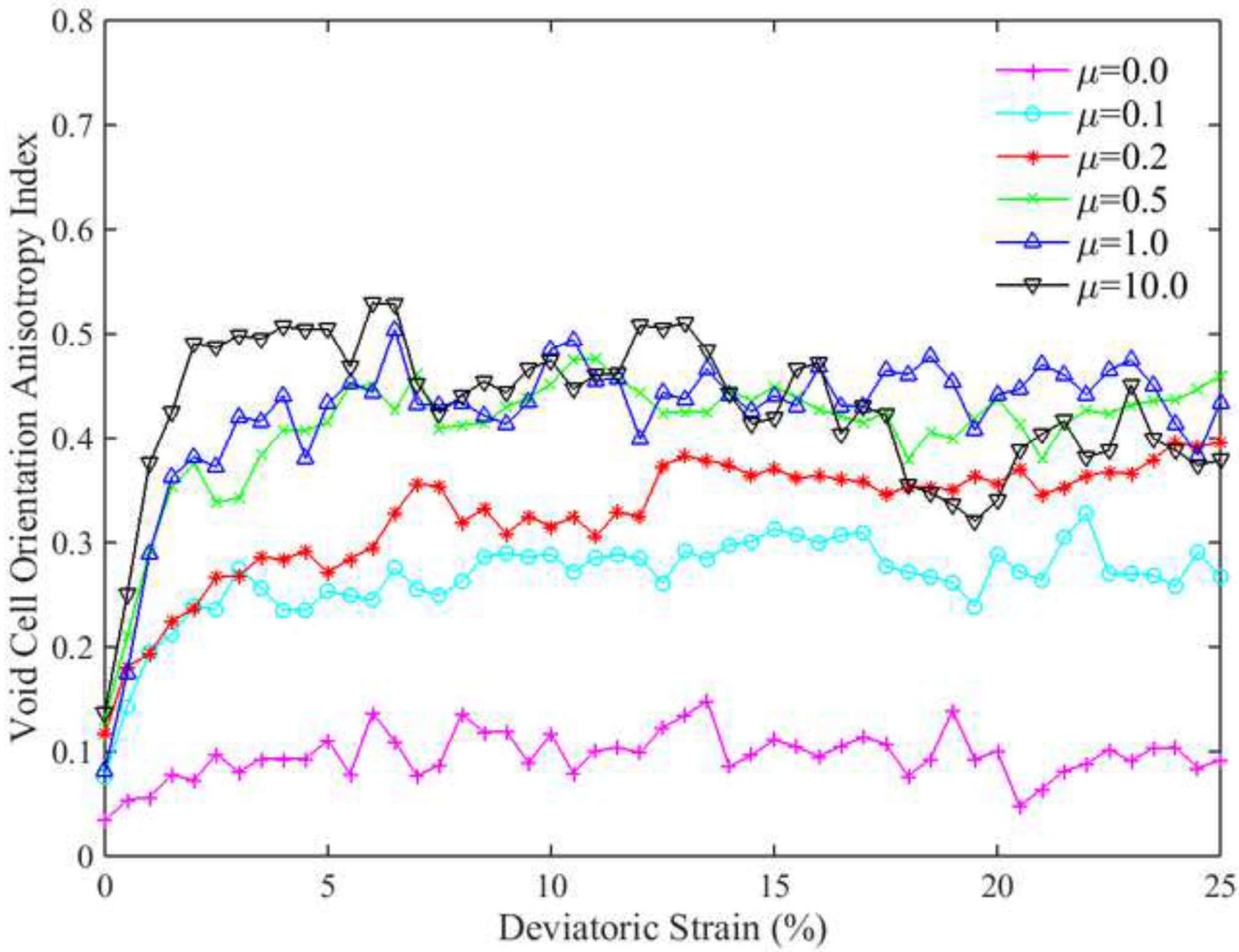

Void Cell Orientation Anisotropy Index
Deviatoric Strain (%)
μ=0.0
μ=0.1
μ=0.2
μ=0.5
μ=1.0
μ=10.0
0
0.1
0.2
0.3
0.4
0.5
0.6
0.7
0.8
0
5
10
15
20
25

Click here to download Figure Fig-10.tif

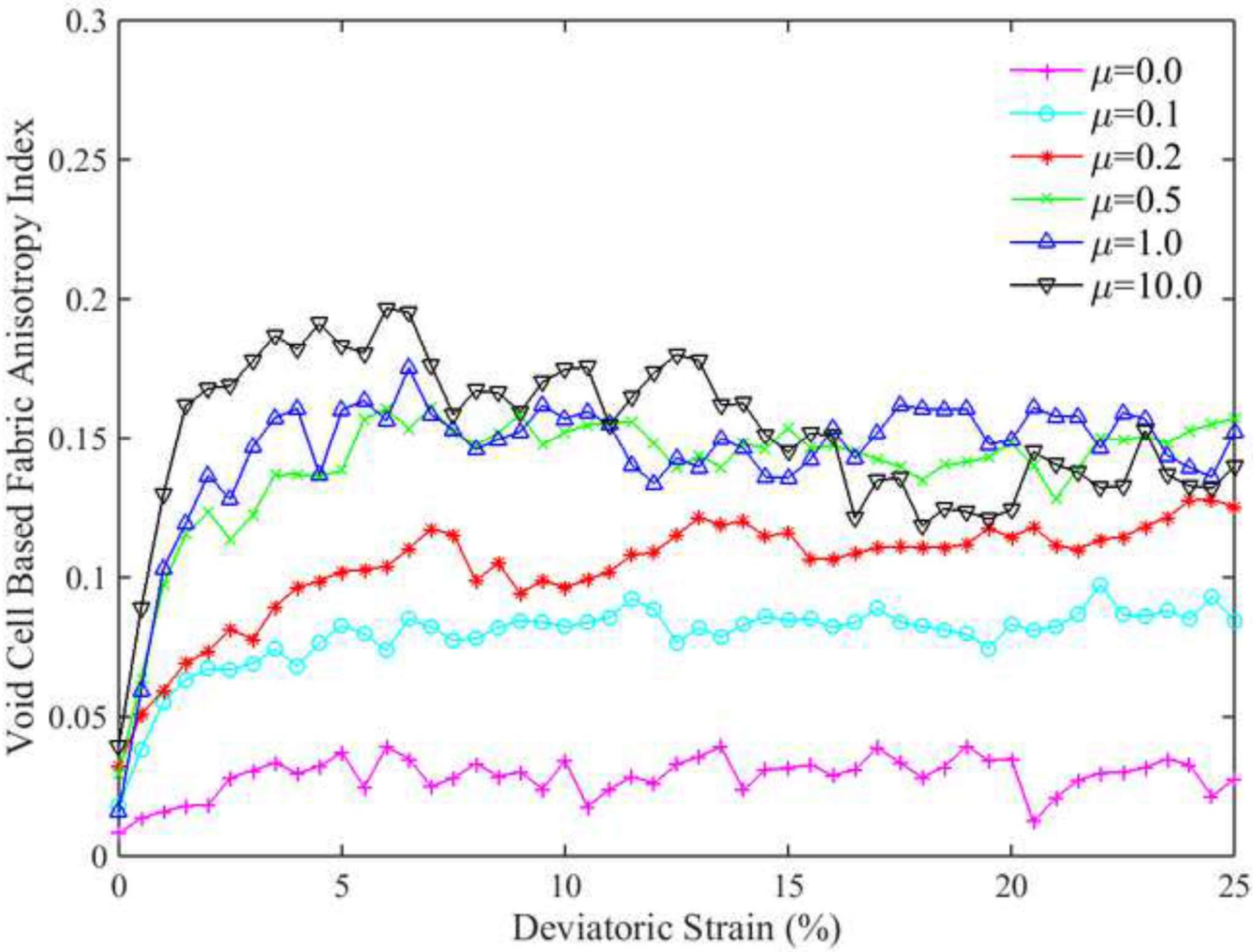

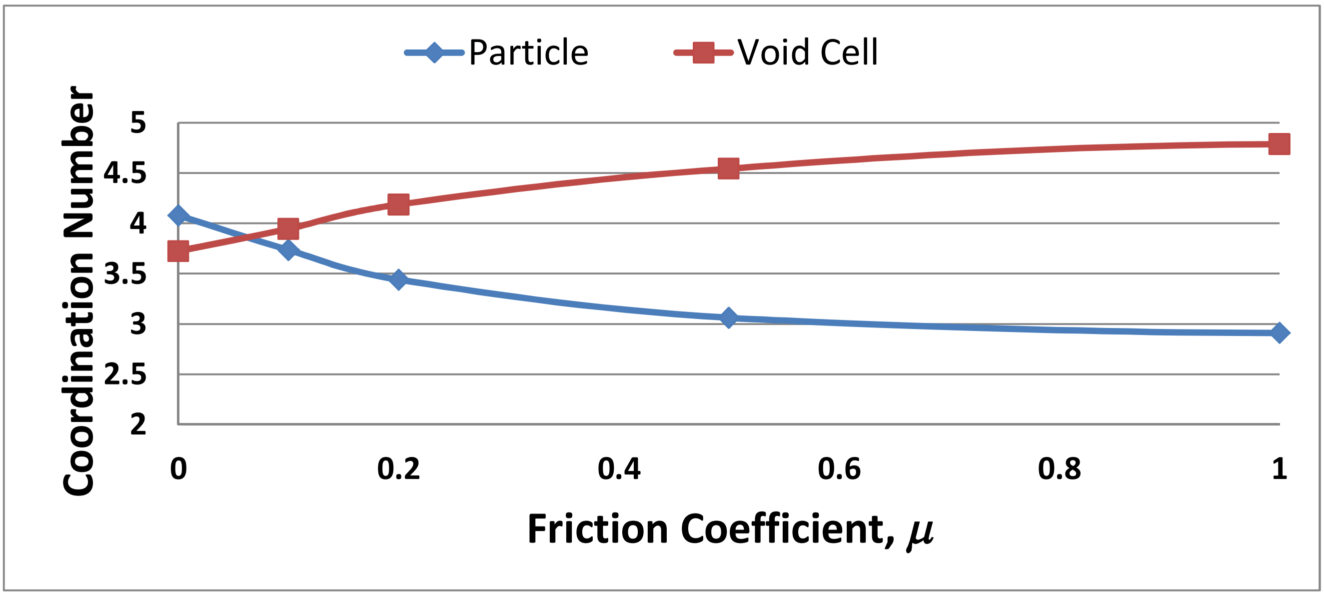
Particle
Void Cell
Coordination Number
5
4.5
4
3.5
3
2.5
2
0
0.2
0.4
0.6
0.8
1
Friction Coefficient, μ

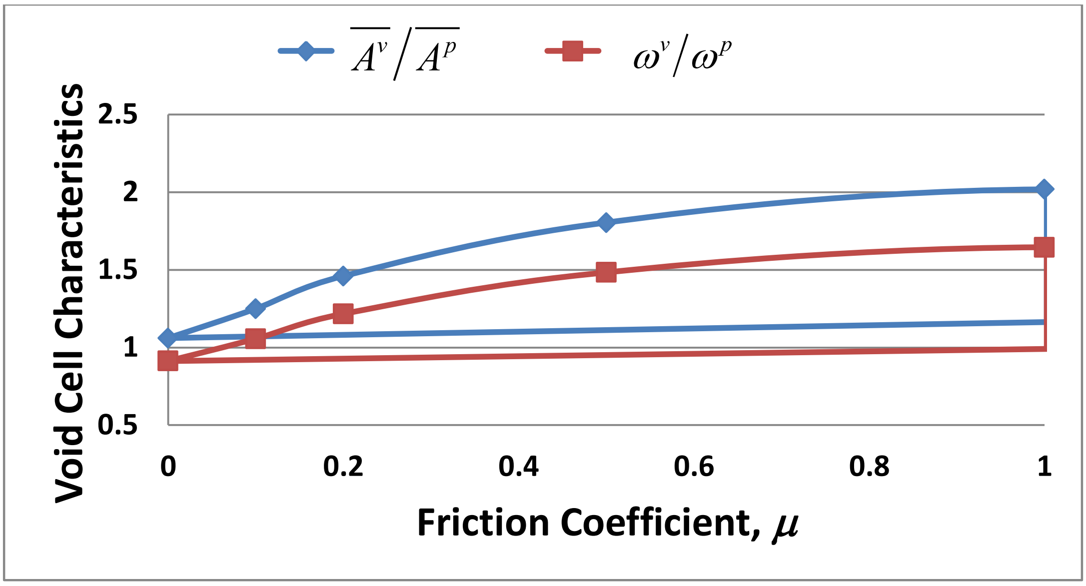

$\overline{A^v}/\overline{A^p}$
ω^v/ω^p
Void Cell Characteristics
2.5
2
1.5
1
0.5
0
0.2
0.4
0.6
0.8
1
Friction Coefficient, μ

Click here to download Figure Fig-12a.tif

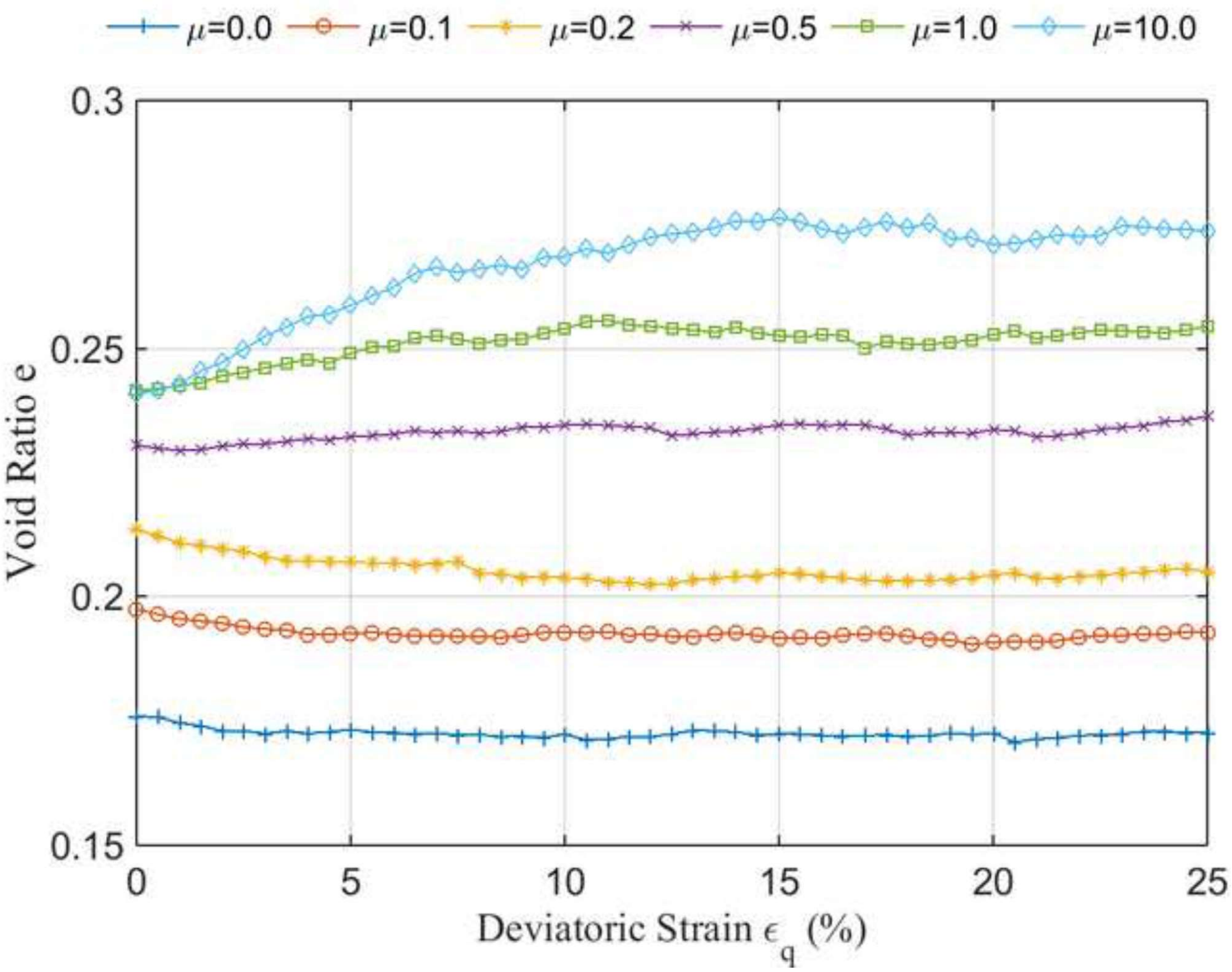

Click here to download Figure Fig-12b.tif

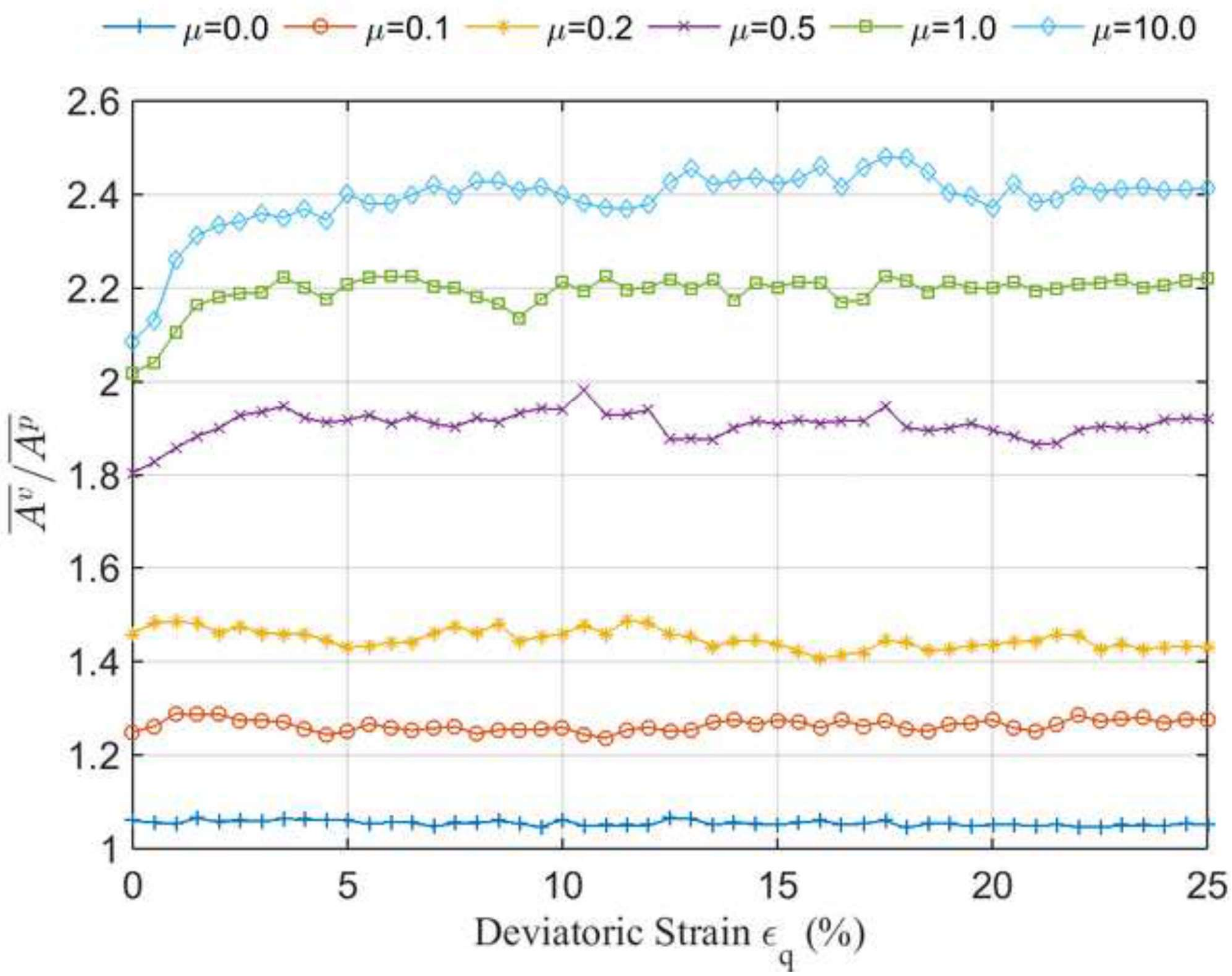

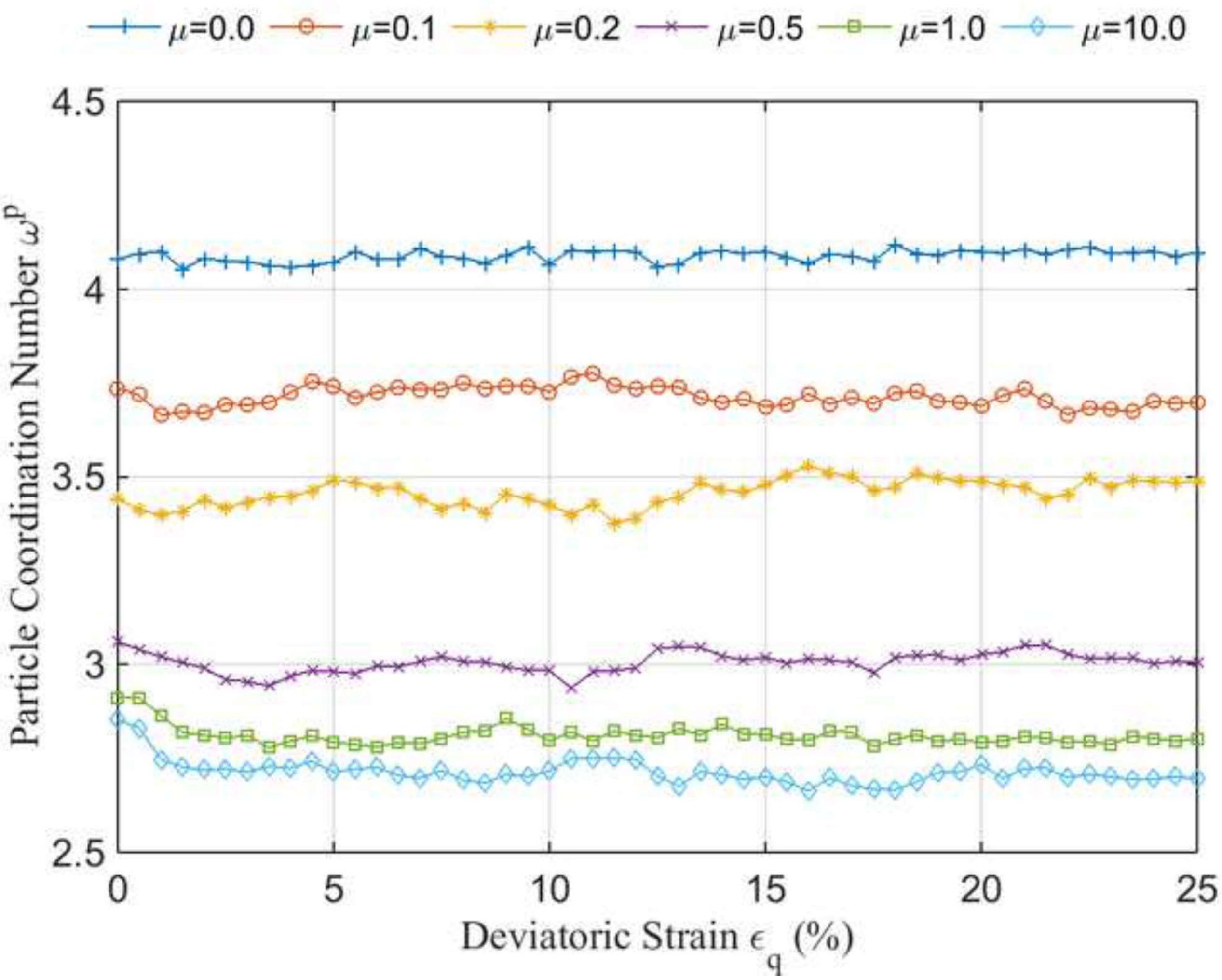

μ=0.0
μ=0.1
μ=0.2
μ=0.5
μ=1.0
μ=10.0
Particle Coordination Number ω^p
Deviatoric Strain ϵ_q (%)
4.5
4
3.5
3
2.5
0
5
10
15
20
25

Click here to download Figure Fig-12d.tif

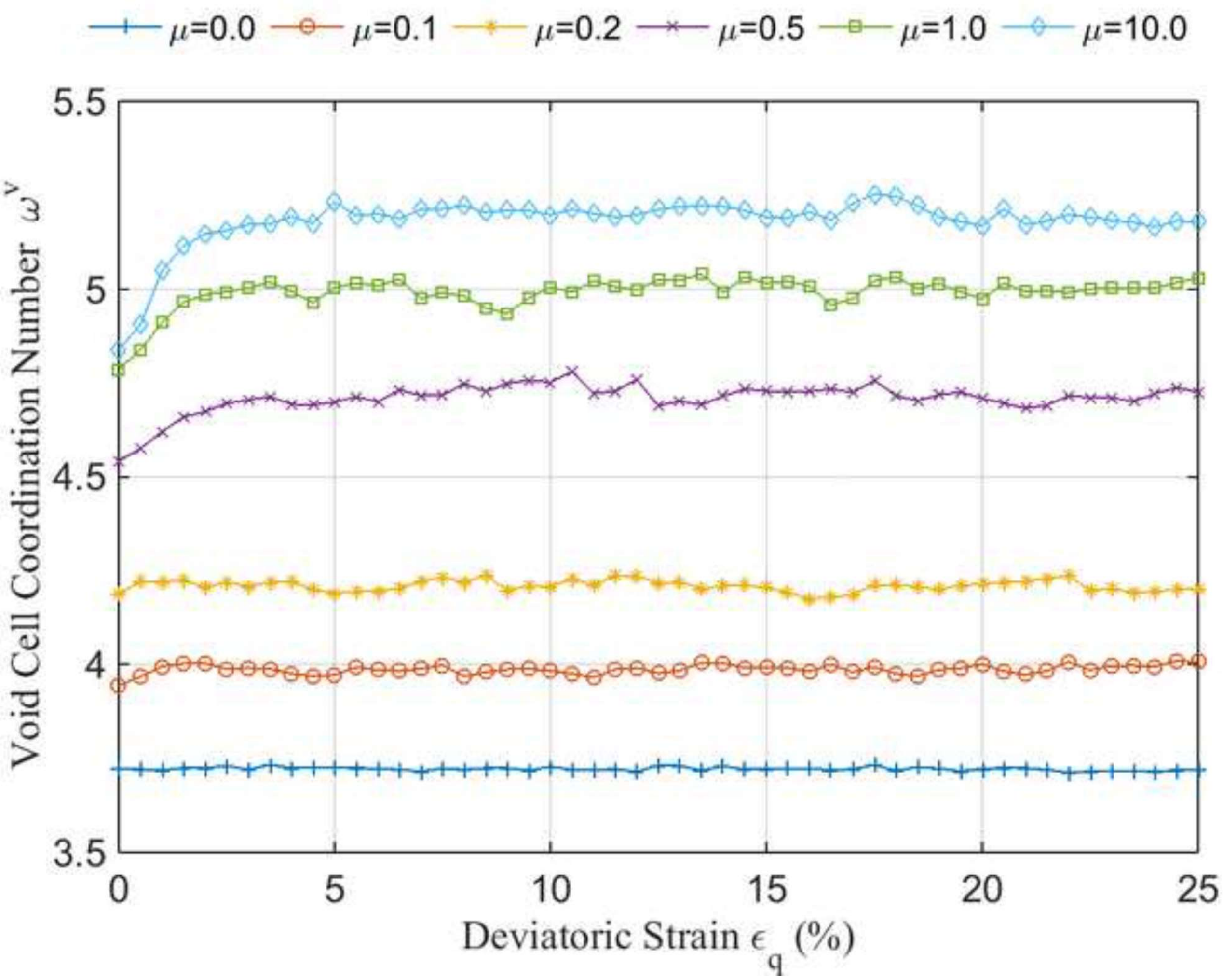

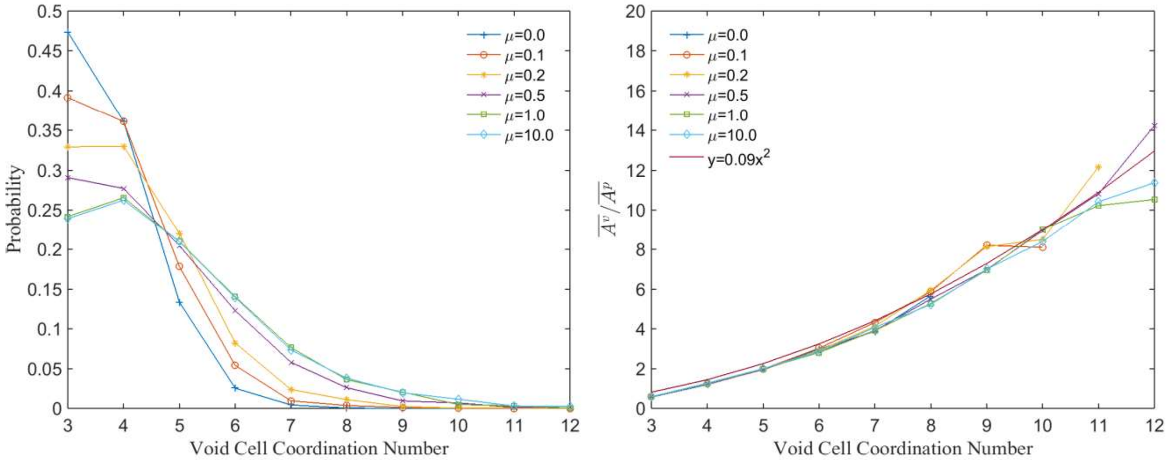
Probability
Void Cell Coordination Number
μ=0.0
μ=0.1
μ=0.2
μ=0.5
μ=1.0
μ=10.0
$\overline{A^v}/\overline{A^p}$
y=0.09x^2

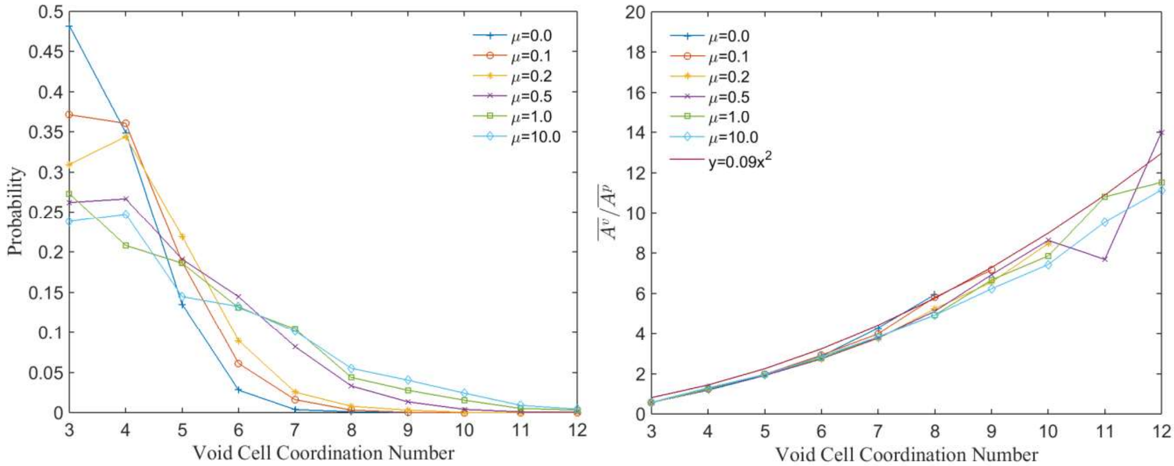

Probability
Void Cell Coordination Number
μ=0.0
μ=0.1
μ=0.2
μ=0.5
μ=1.0
μ=10.0
$\overline{A^v}/\overline{A^p}$
Void Cell Coordination Number
μ=0.0
μ=0.1
μ=0.2
μ=0.5
μ=1.0
μ=10.0
y=0.09x2

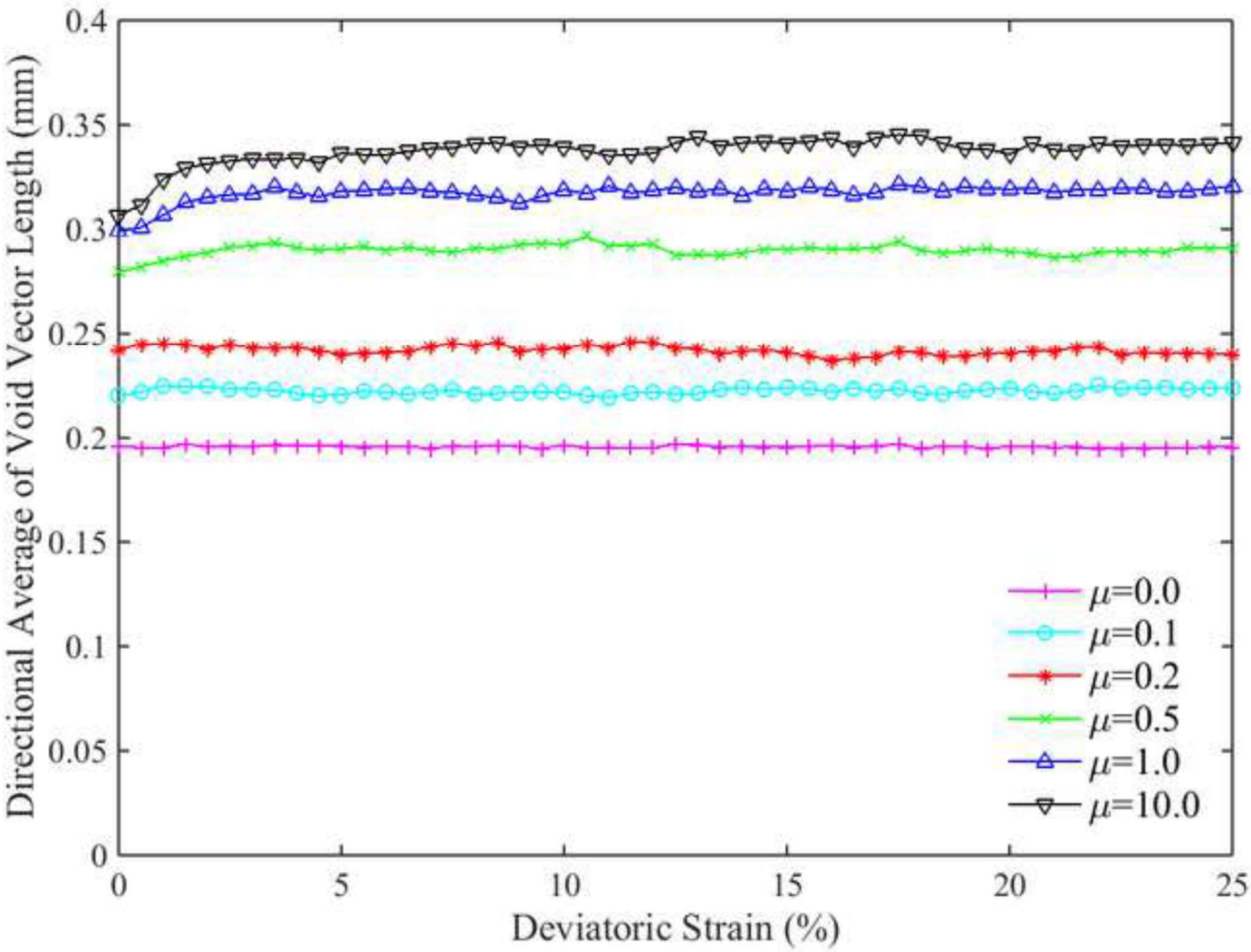

Directional Average of Void Vector Length (mm)
0.4
0.35
0.3
0.25
0.2
0.15
0.1
0.05
0
0
5
10
15
20
25
Deviatoric Strain (%)
μ=0.0
μ=0.1
μ=0.2
μ=0.5
μ=1.0
μ=10.0

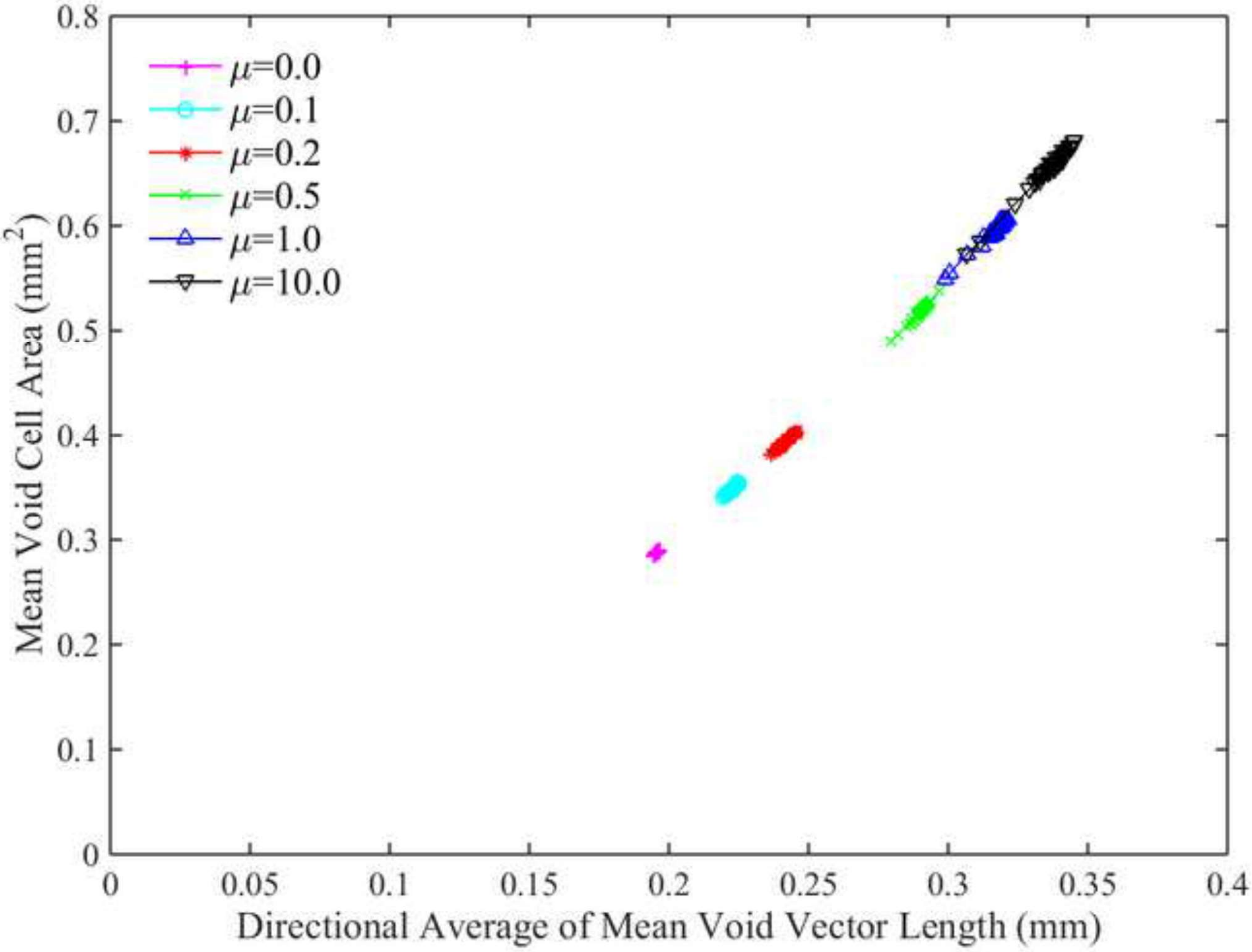

0.8
0.7
0.6
0.5
0.4
0.3
0.2
0.1
0
Mean Void Cell Area (mm^2)
μ=0.0
μ=0.1
μ=0.2
μ=0.5
μ=1.0
μ=10.0
0
0.05
0.1
0.15
0.2
0.25
0.3
0.35
0.4
Directional Average of Mean Void Vector Length (mm)

Click here to download Figure Fig-16a.tif

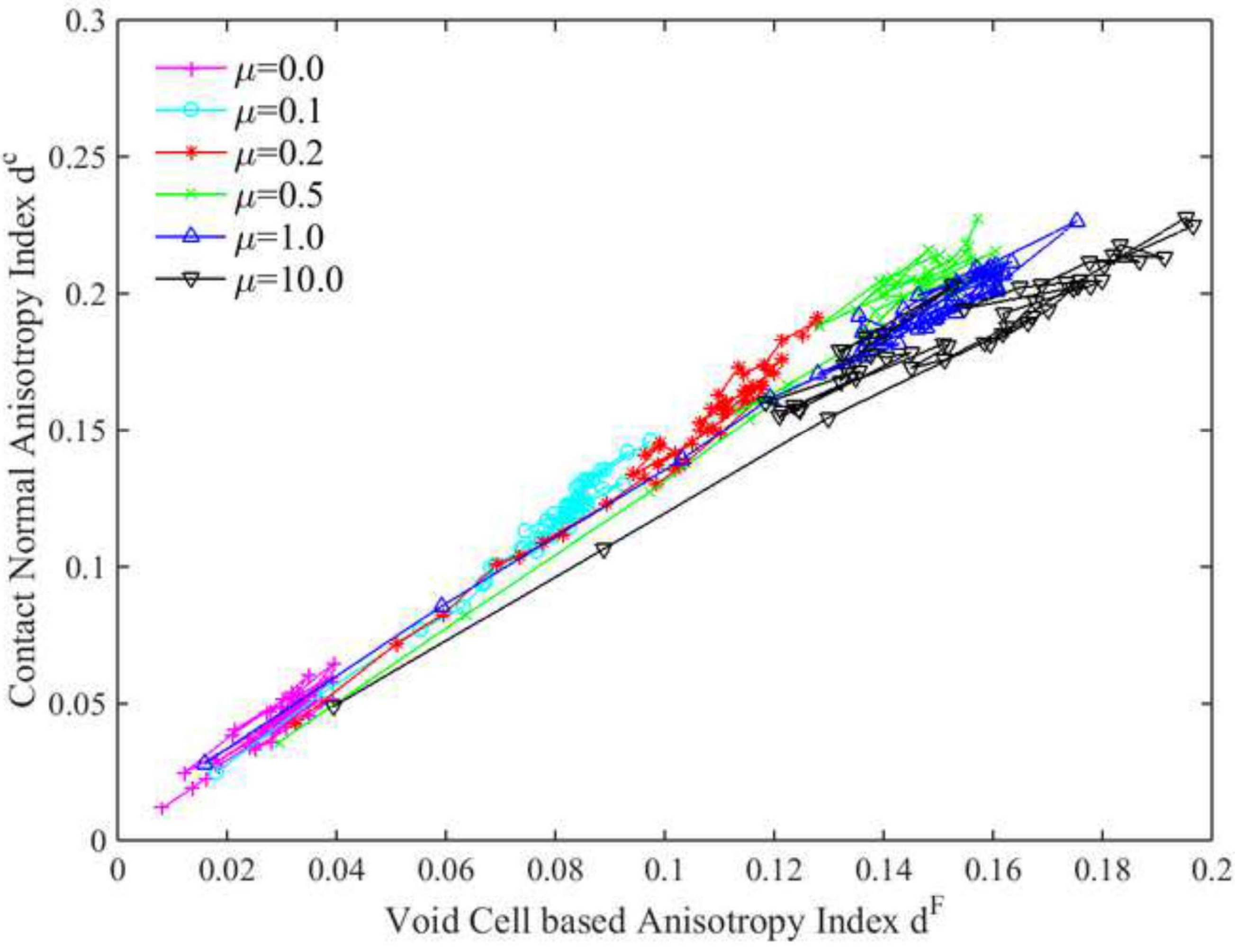

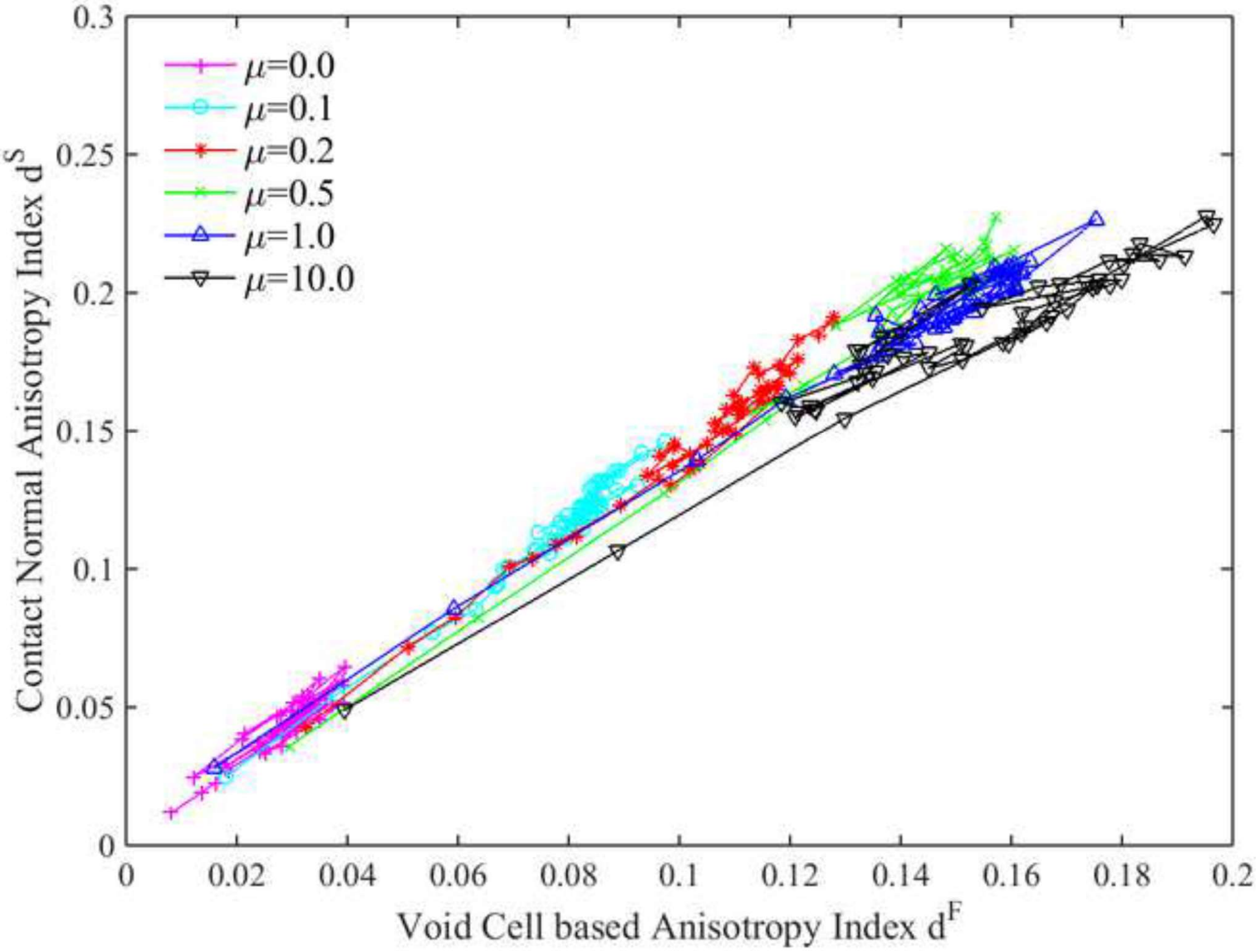

0.3
0.25
0.2
0.15
0.1
0.05
0
0
0.02
0.04
0.06
0.08
0.1
0.12
0.14
0.16
0.18
0.2
μ=0.0
μ=0.1
μ=0.2
μ=0.5
μ=1.0
μ=10.0
Contact Normal Anisotropy Index d^S
Void Cell based Anisotropy Index d^F

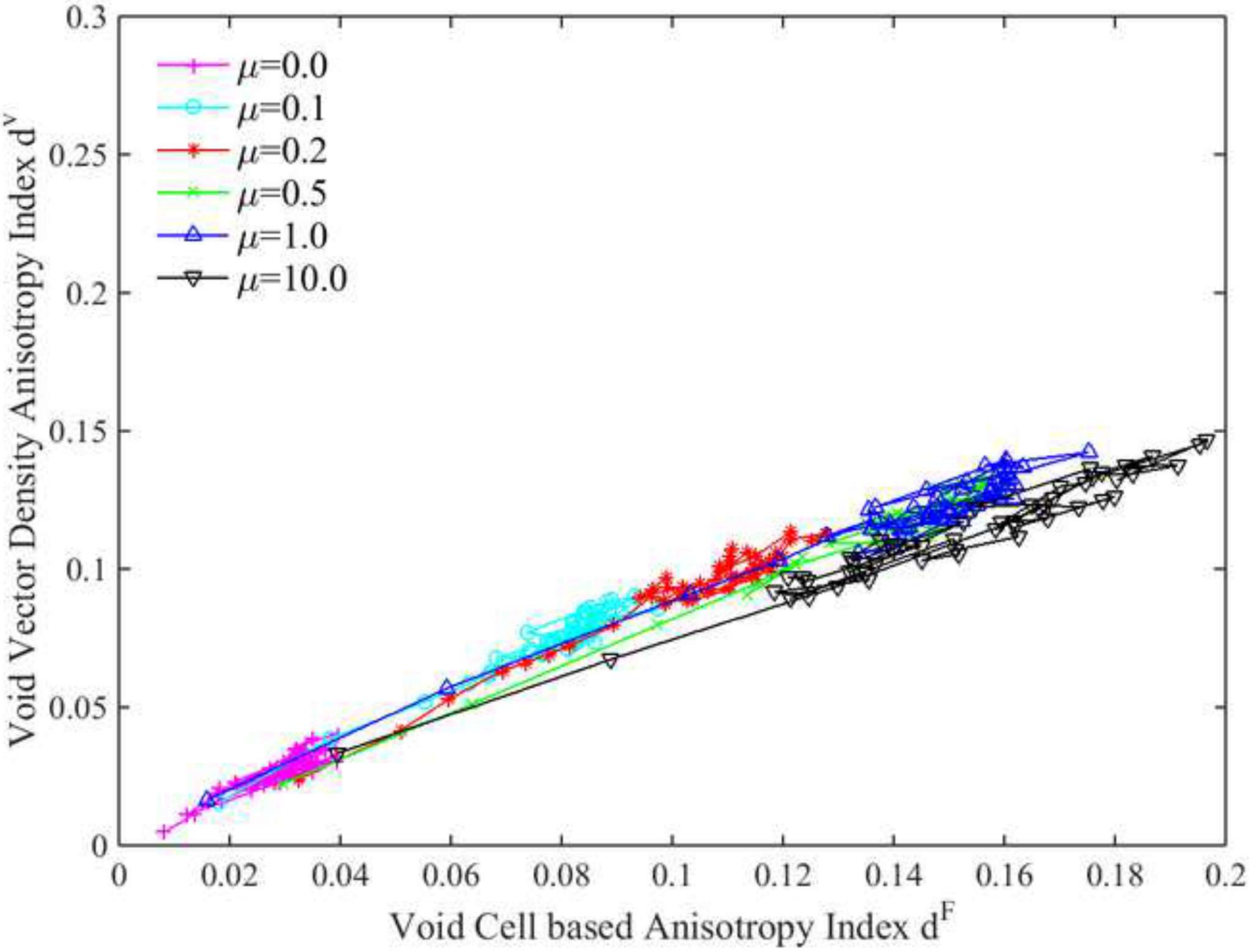

0.3
0.25
0.2
0.15
0.1
0.05
0
0
0.02
0.04
0.06
0.08
0.1
0.12
0.14
0.16
0.18
0.2
μ=0.0
μ=0.1
μ=0.2
μ=0.5
μ=1.0
μ=10.0
Void Vector Density Anisotropy Index d^V
Void Cell based Anisotropy Index d^F

Click here to download Figure Fig-16d.tif

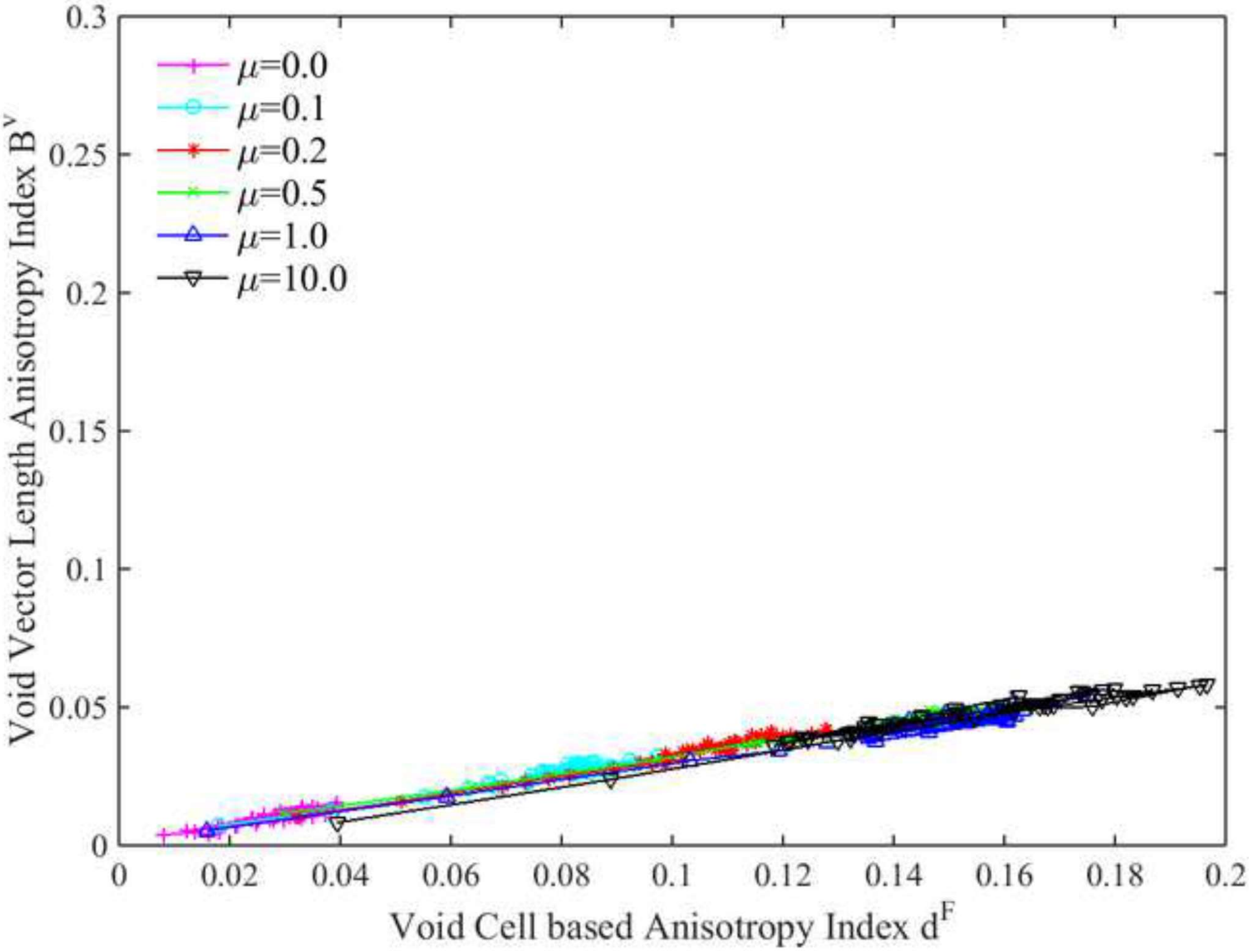

Figure

Click here to download Figure Fig-17a.pdf

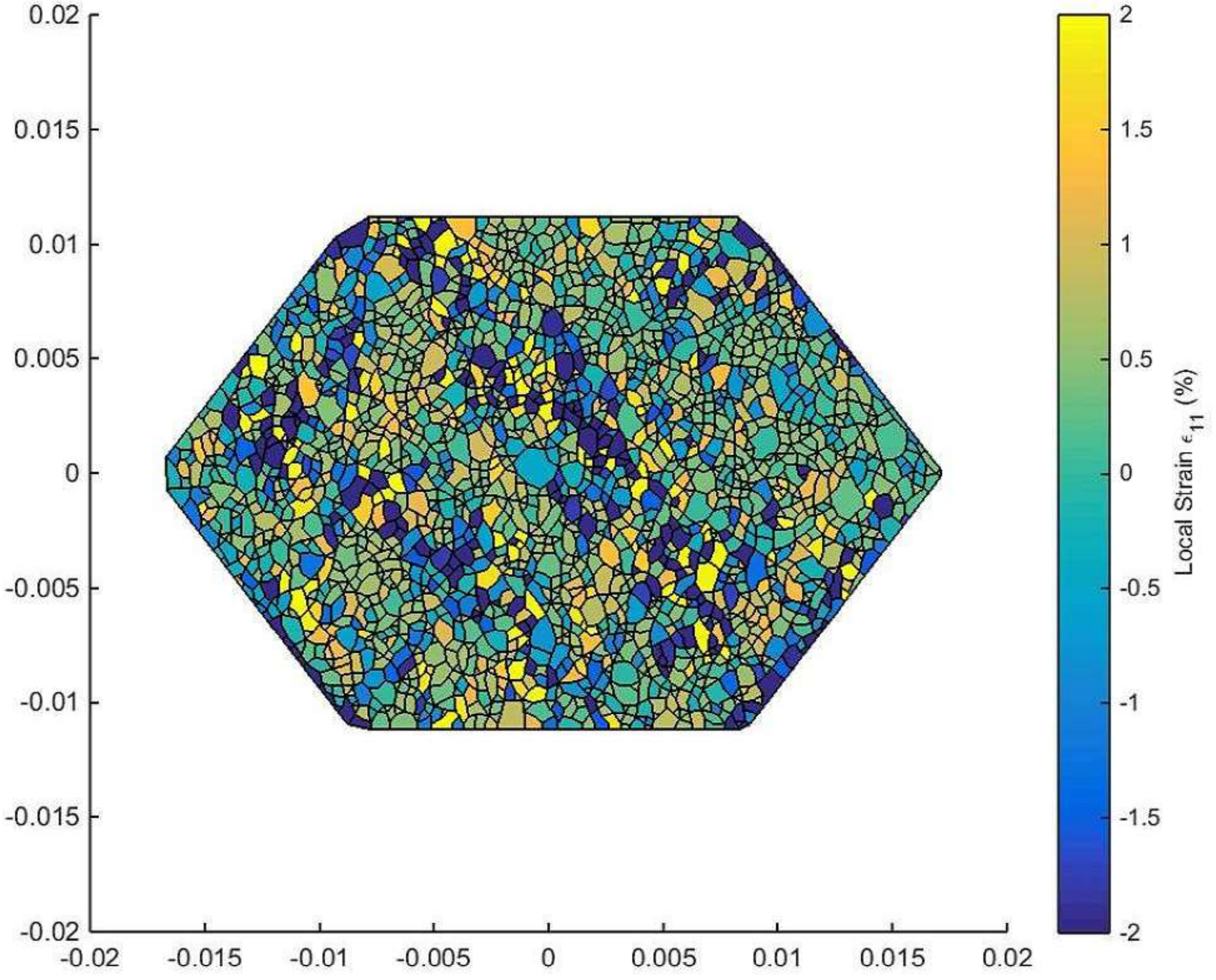

Figure

Click here to download Figure Fig-17b.pdf

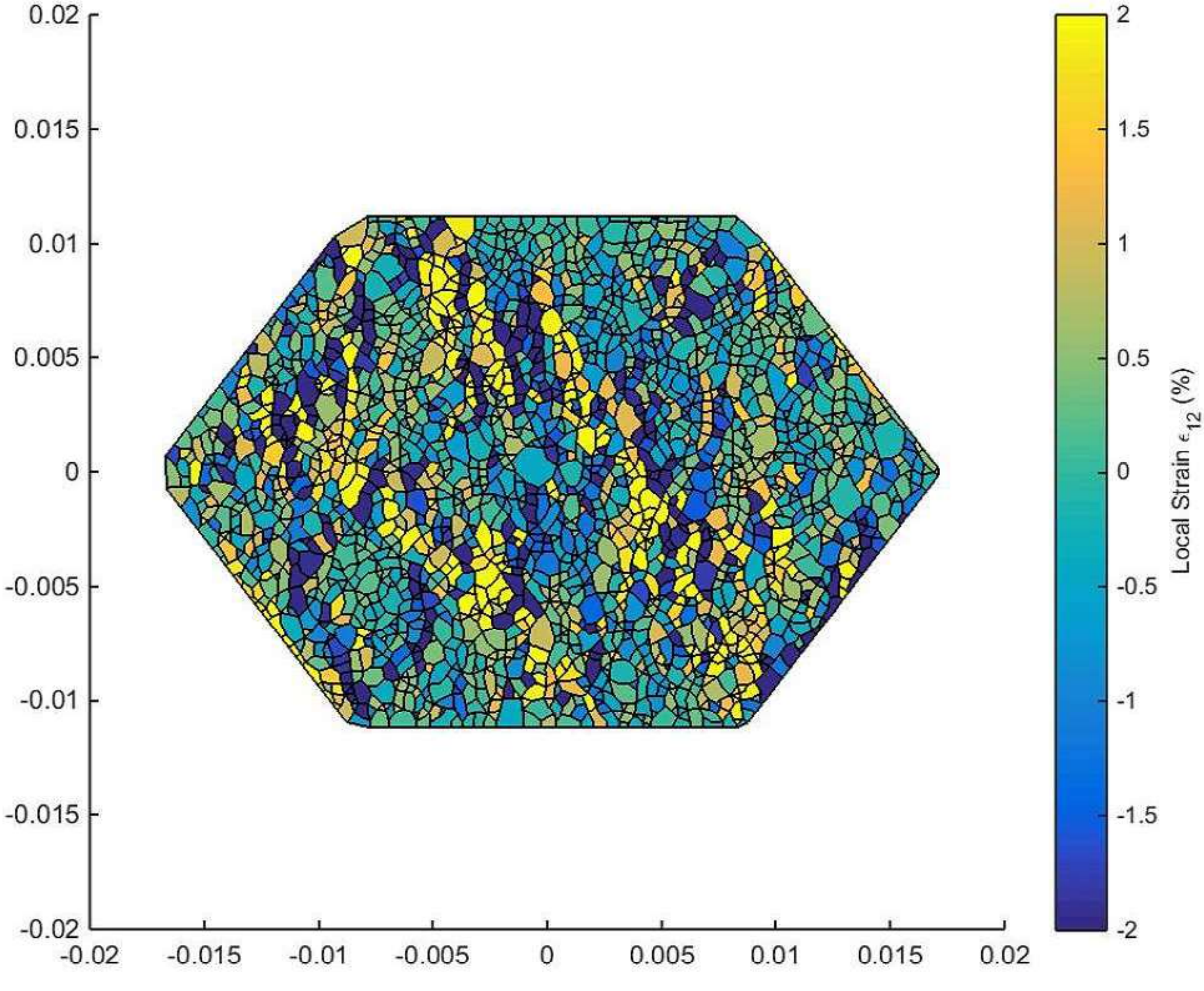

Figure

Click here to download Figure Fig-17c.pdf

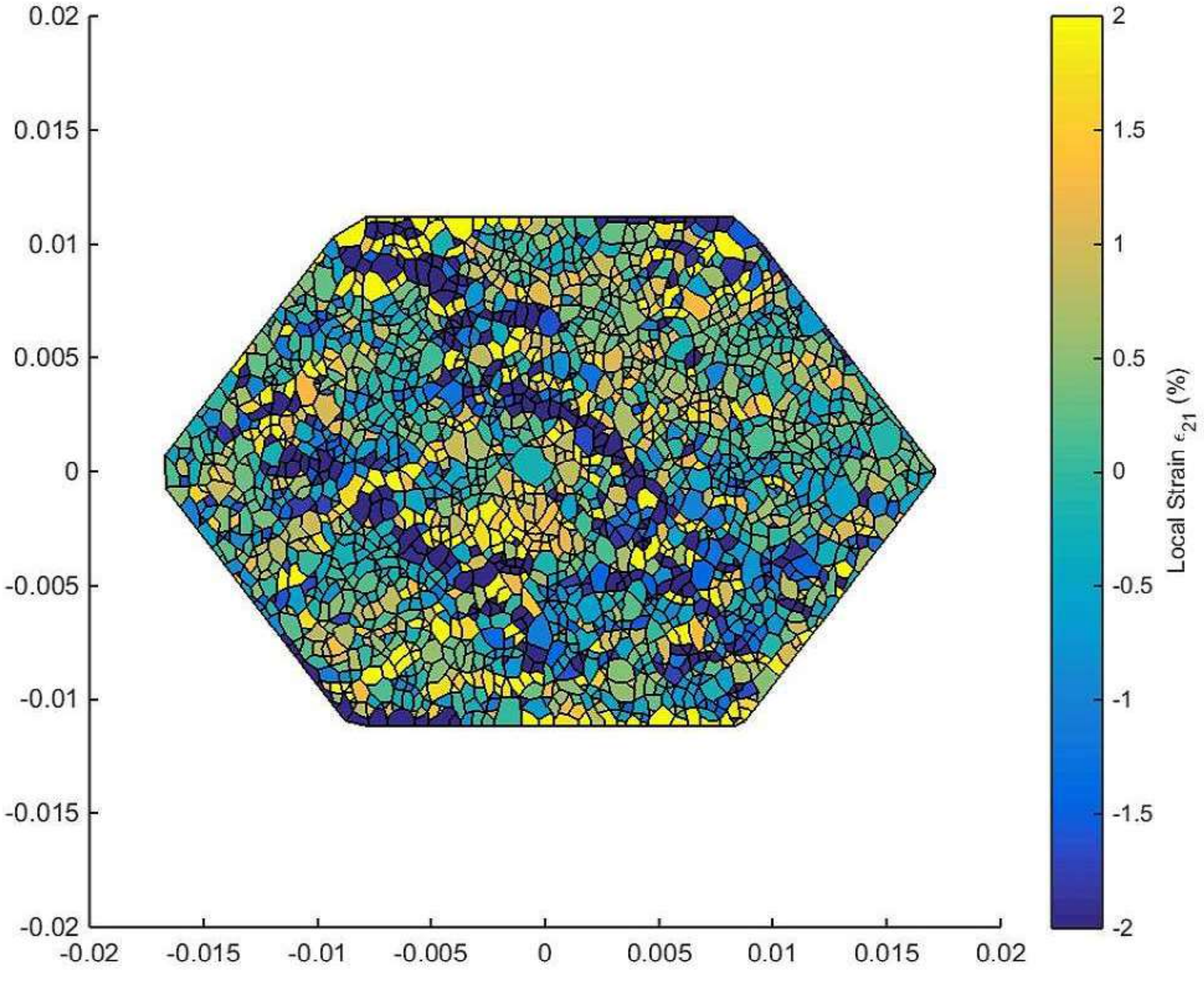

Figure

Click here to download Figure Fig-17d.pdf

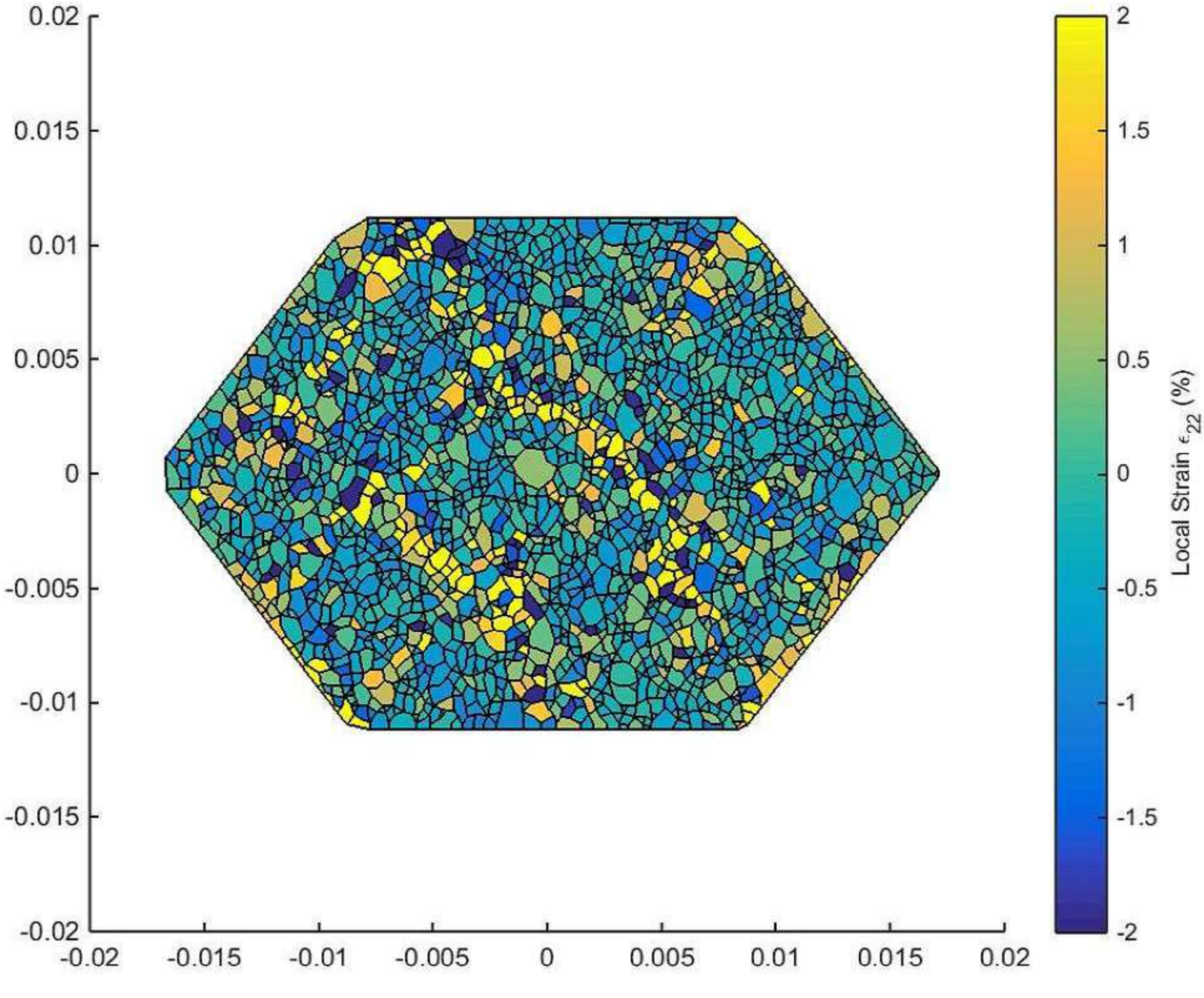

Figure

Click here to download Figure Fig-18a.tiff

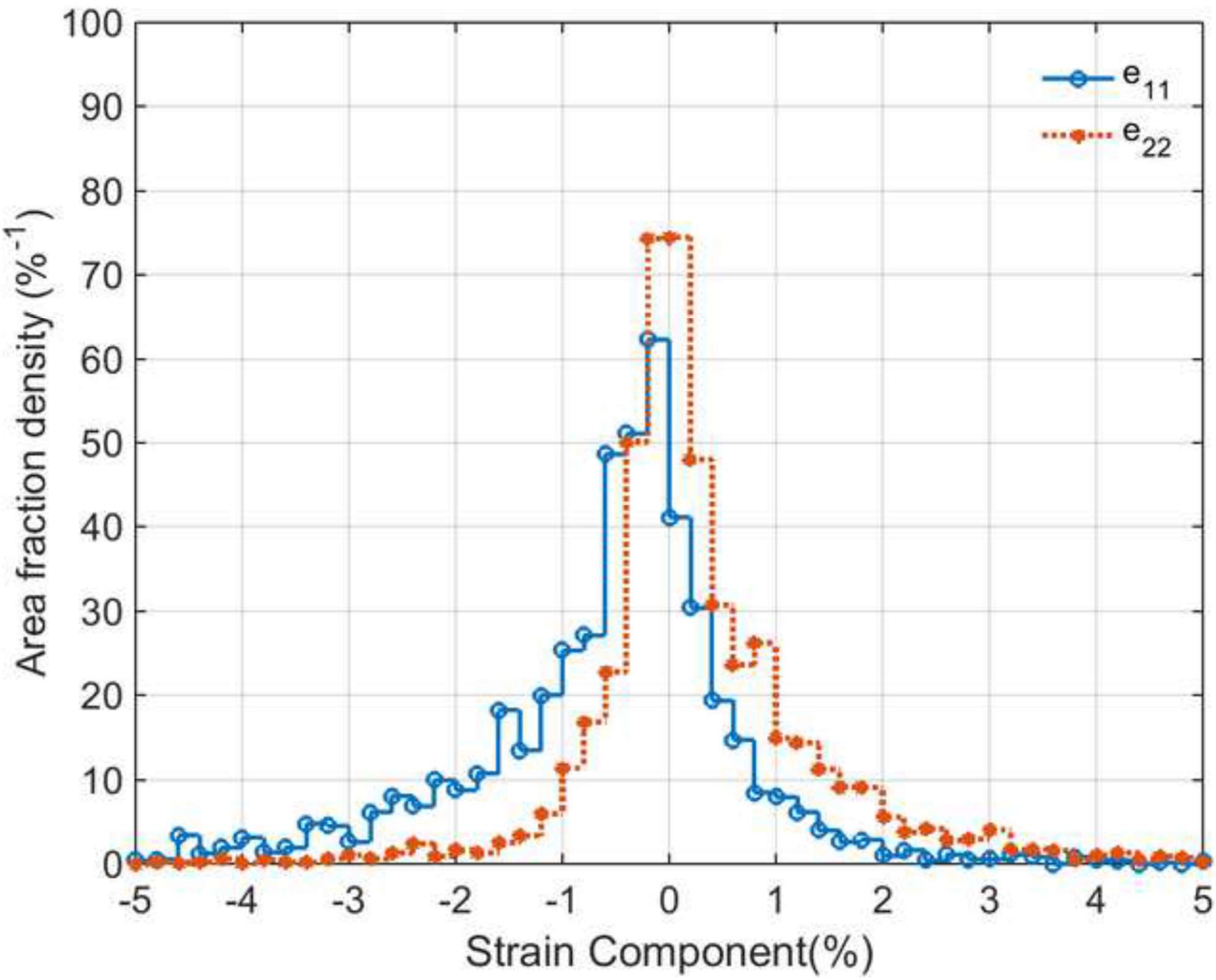

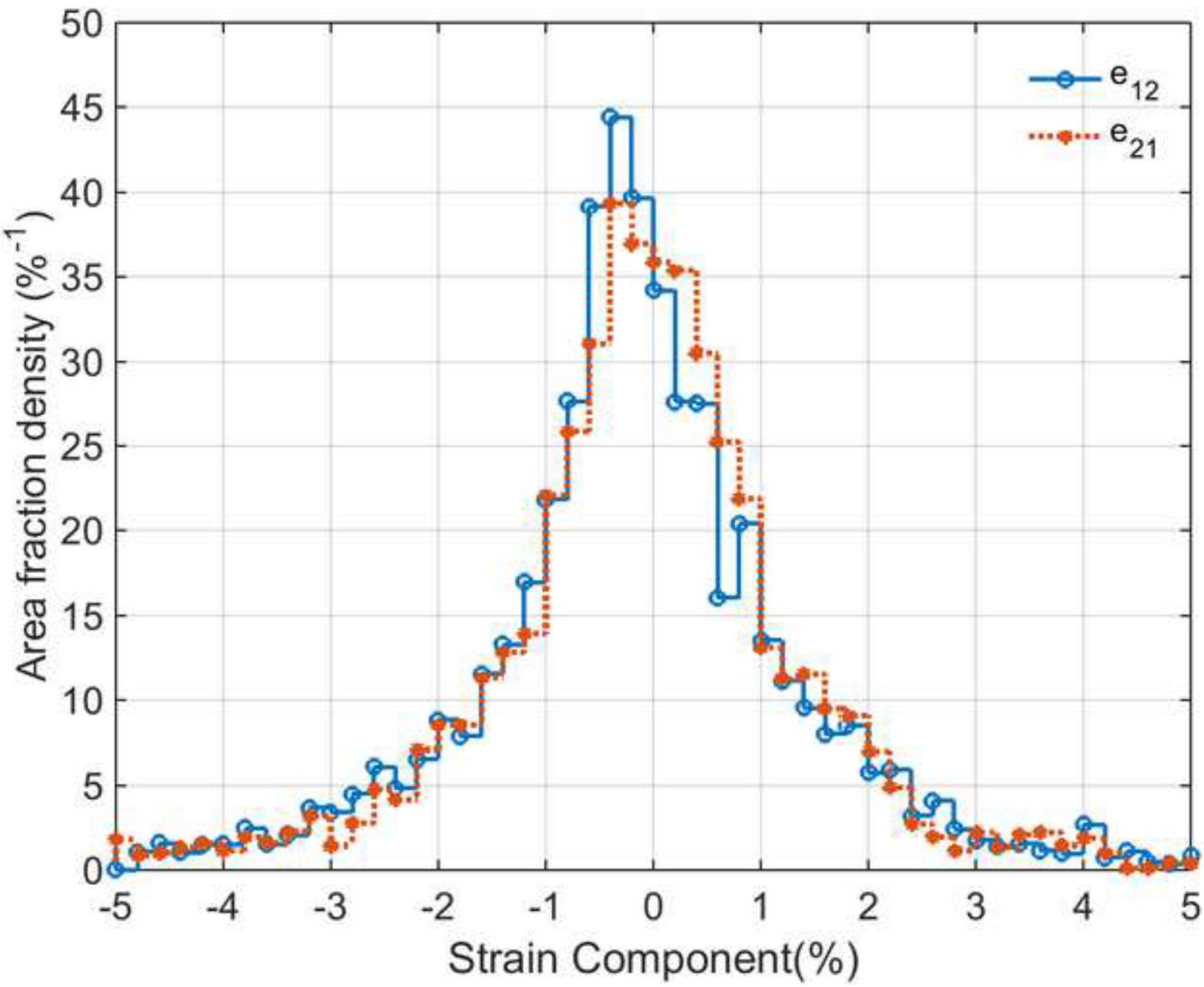

e12
e21
Area fraction density (%^-1)
Strain Component(%)
0
5
10
15
20
25
30
35
40
45
50
-5
-4
-3
-2
-1
0
1
2
3
4
5

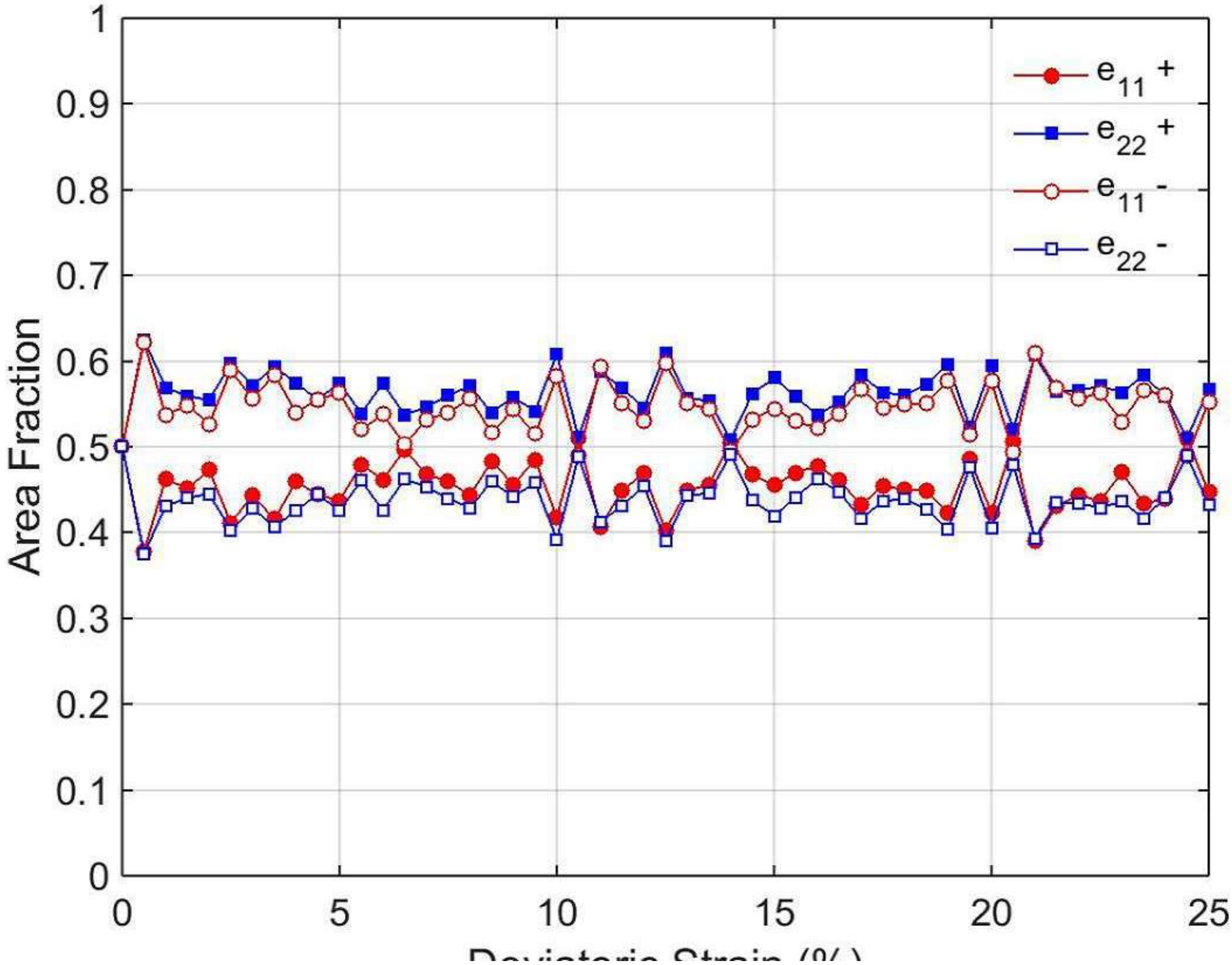
Area Fraction
Deviatoric Strain (%)
0
0.1
0.2
0.3
0.4
0.5
0.6
0.7
0.8
0.9
1
0
5
10
15
20
25
e11 +
e22 +
e11 -
e22 -

Figure

Click here to download Figure Fig-19a-2.pdf

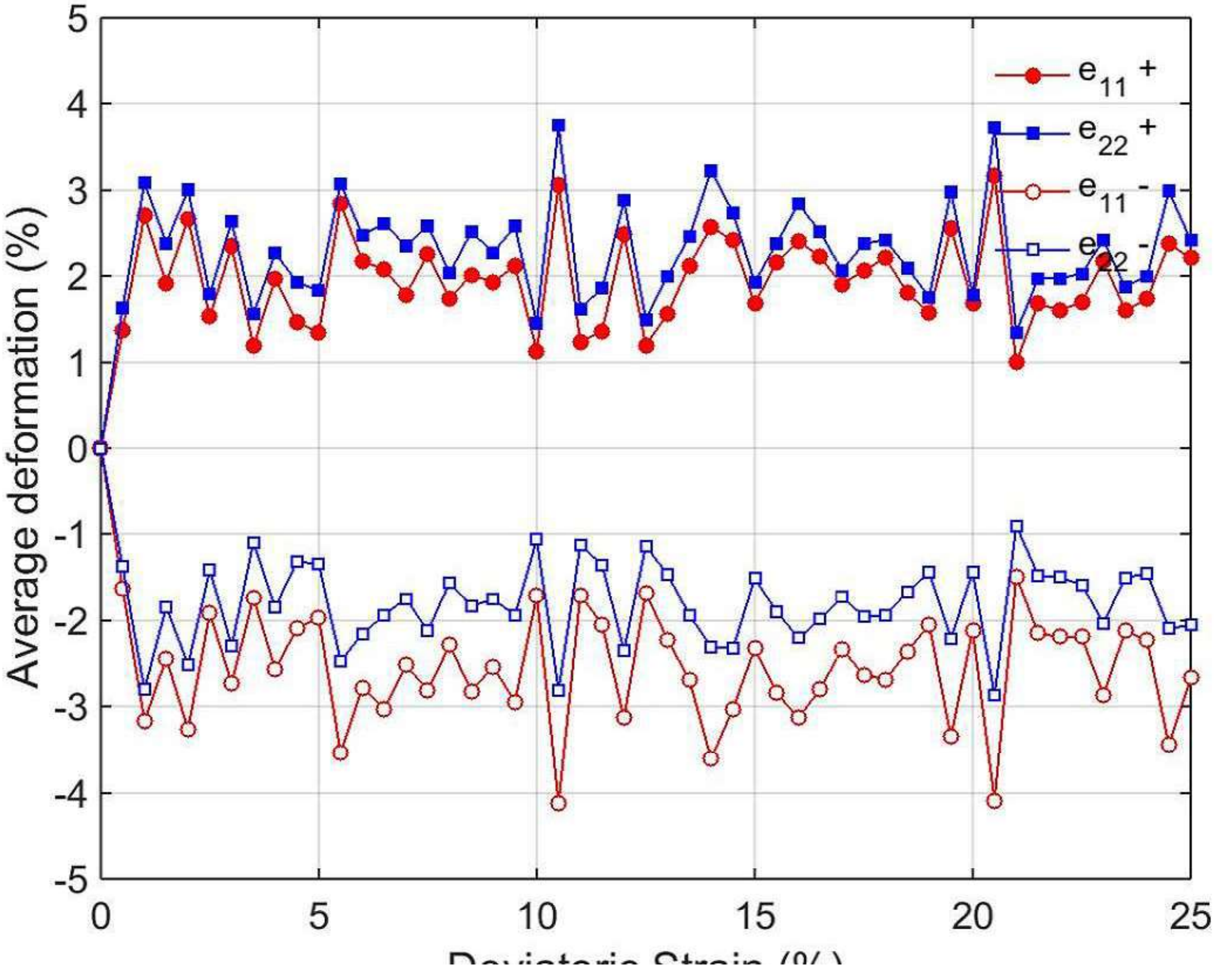

Figure

Click here to download Figure Fig-19a-3.pdf

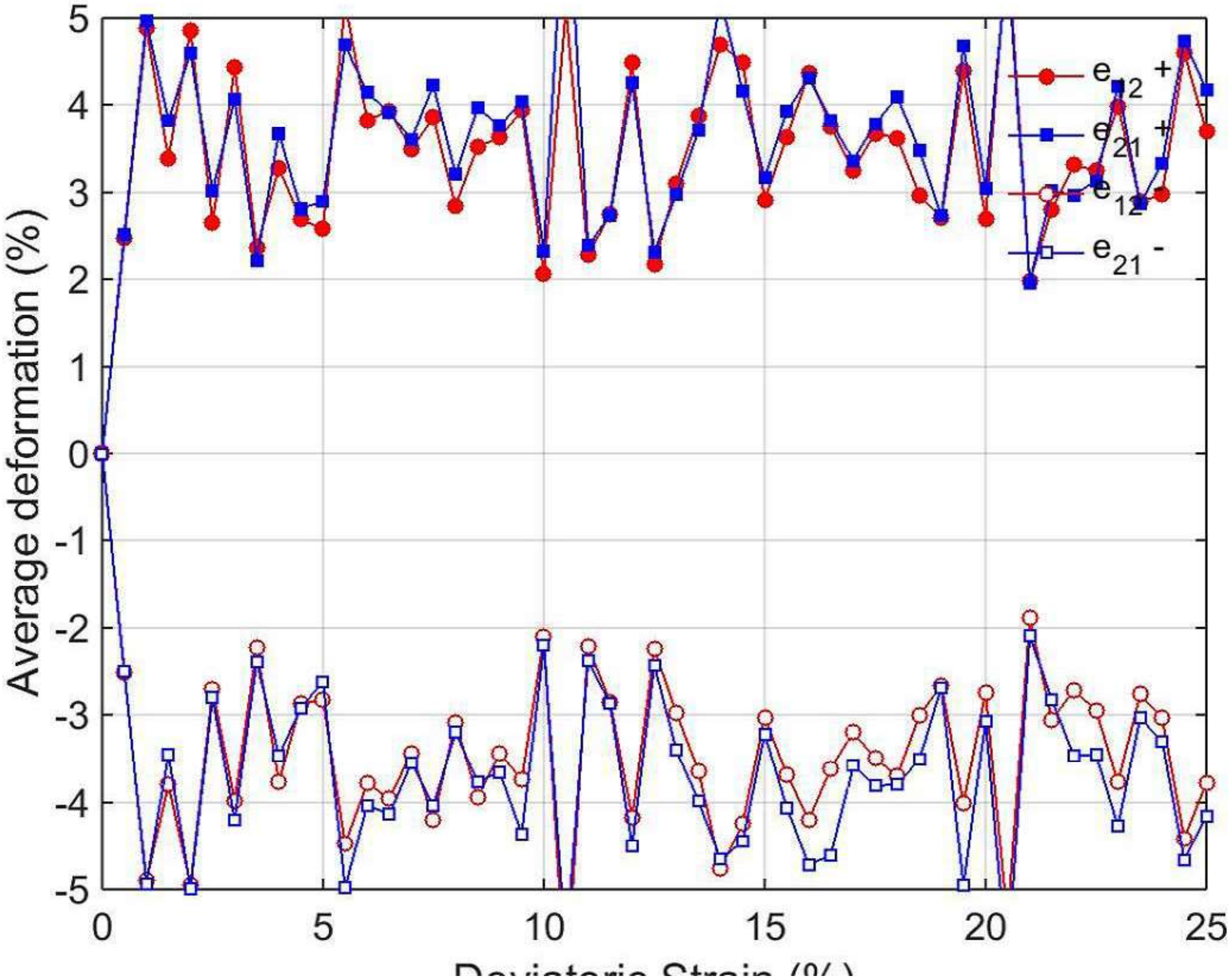

Figure

Click here to download Figure Fig-19b-1.pdf

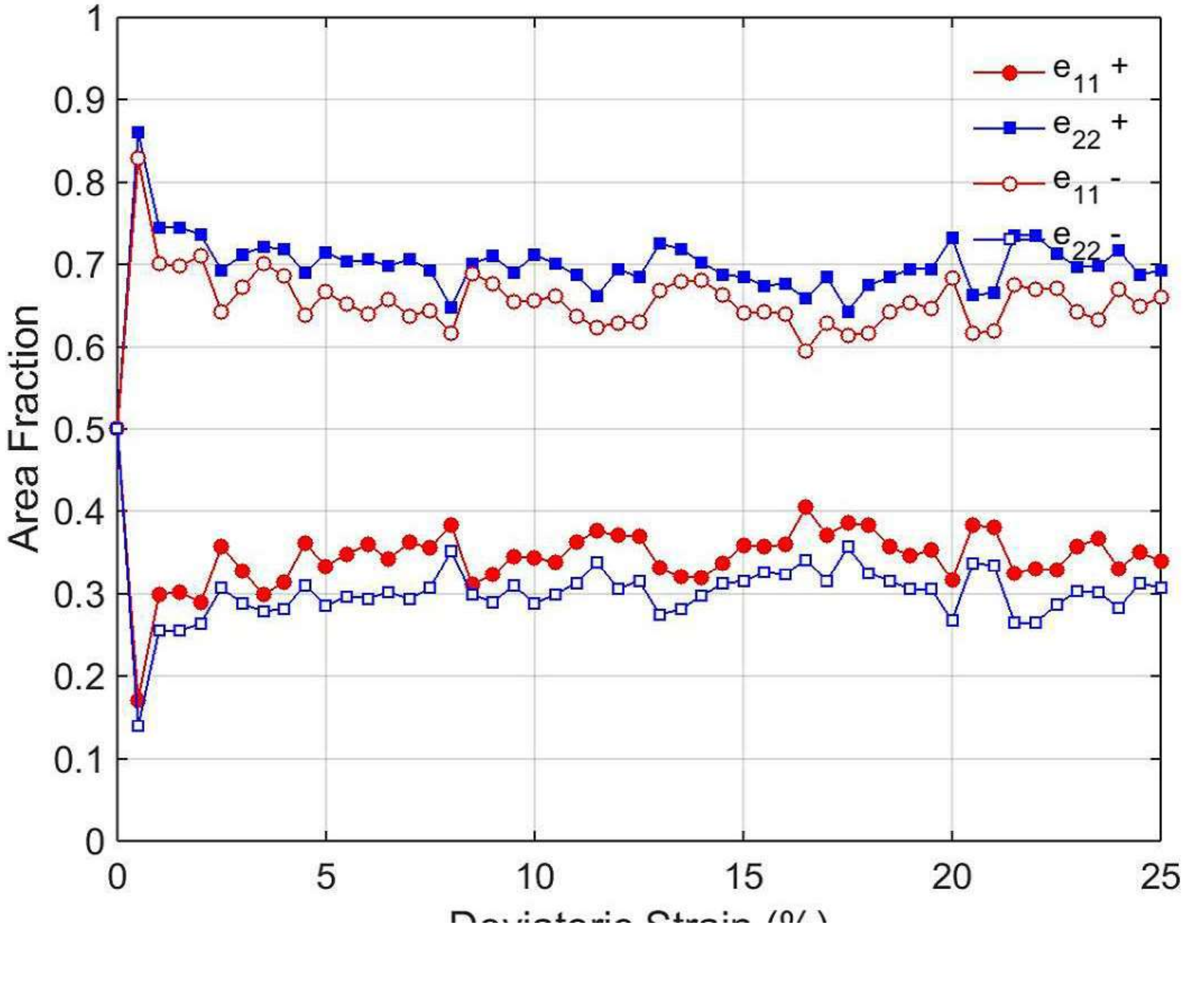

Figure

Click here to download Figure Fig-19b-2.pdf

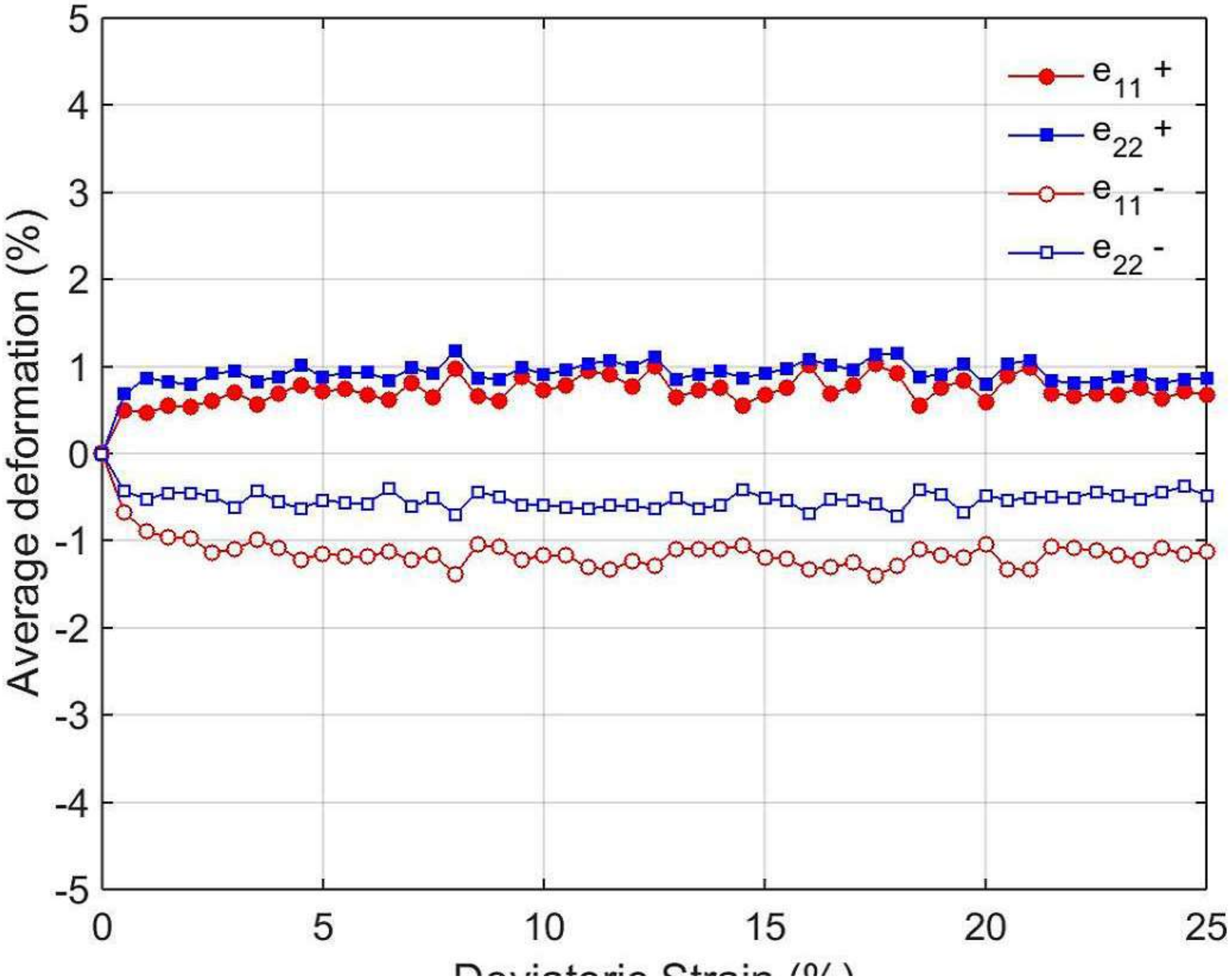

Figure

Click here to download Figure Fig-19b-3.pdf

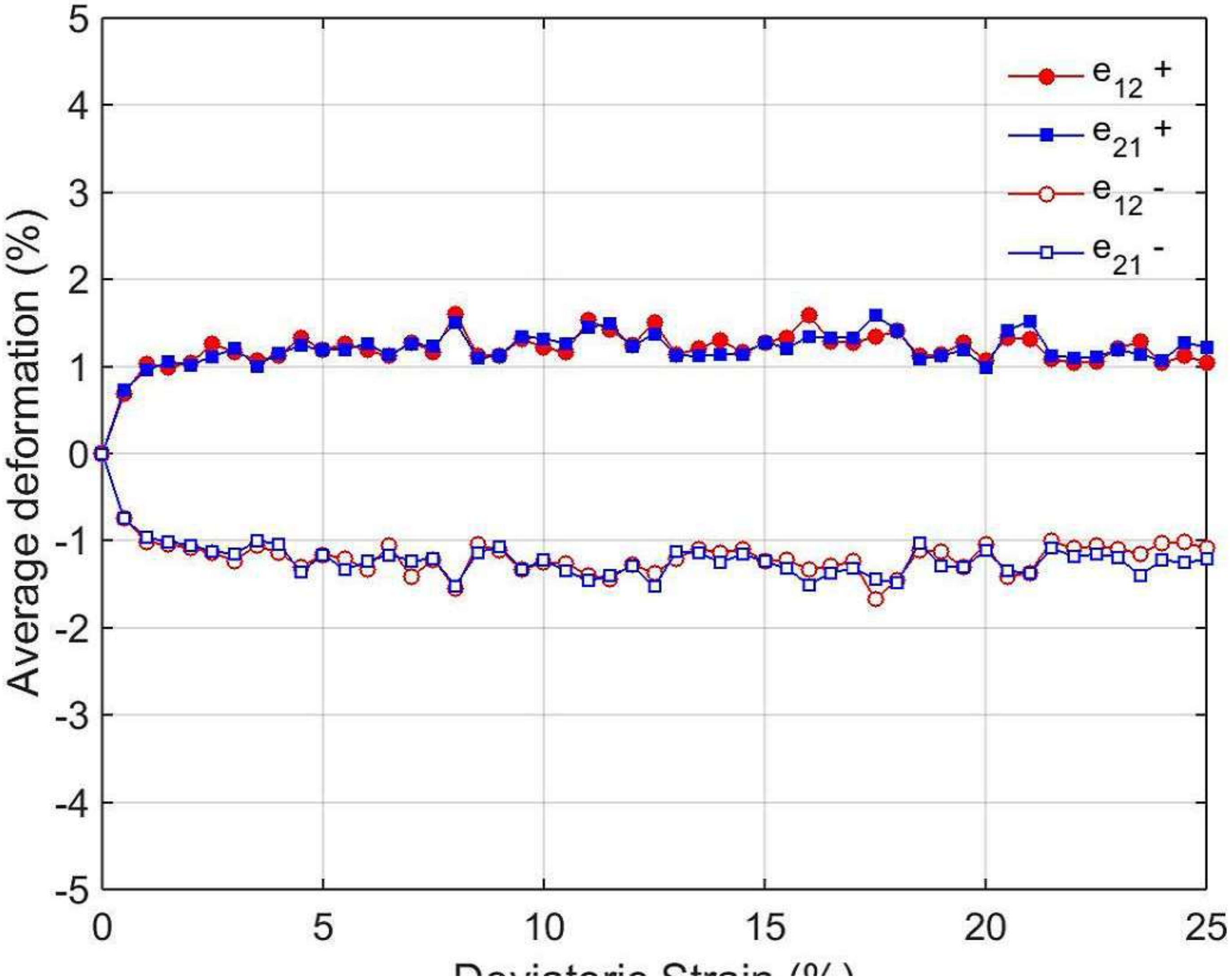

Figure

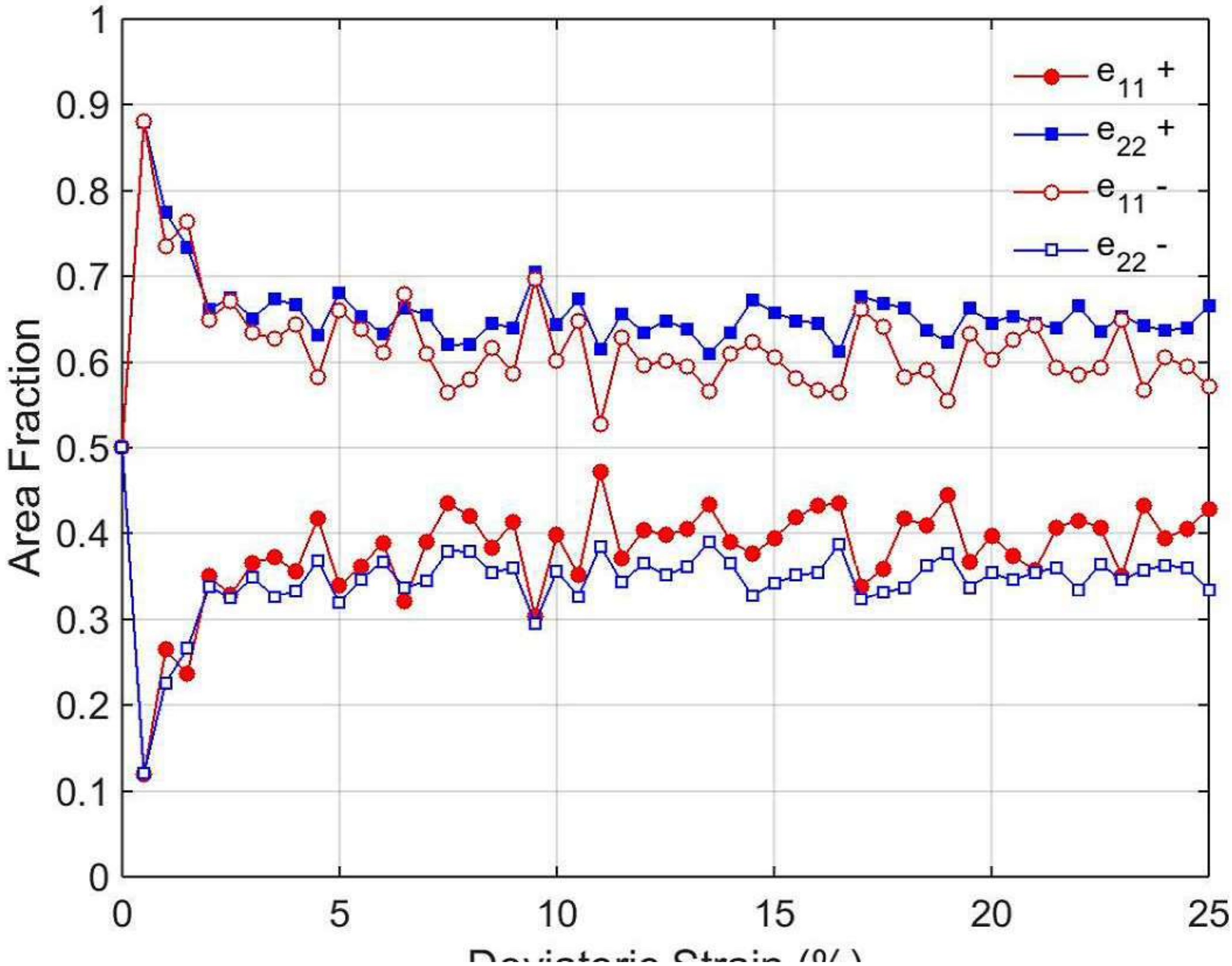

1
0.9
0.8
0.7
0.6
0.5
0.4
0.3
0.2
0.1
0
Area Fraction
0
5
10
15
20
25
e11 +
e22 +
e11 -
e22 -

Figure

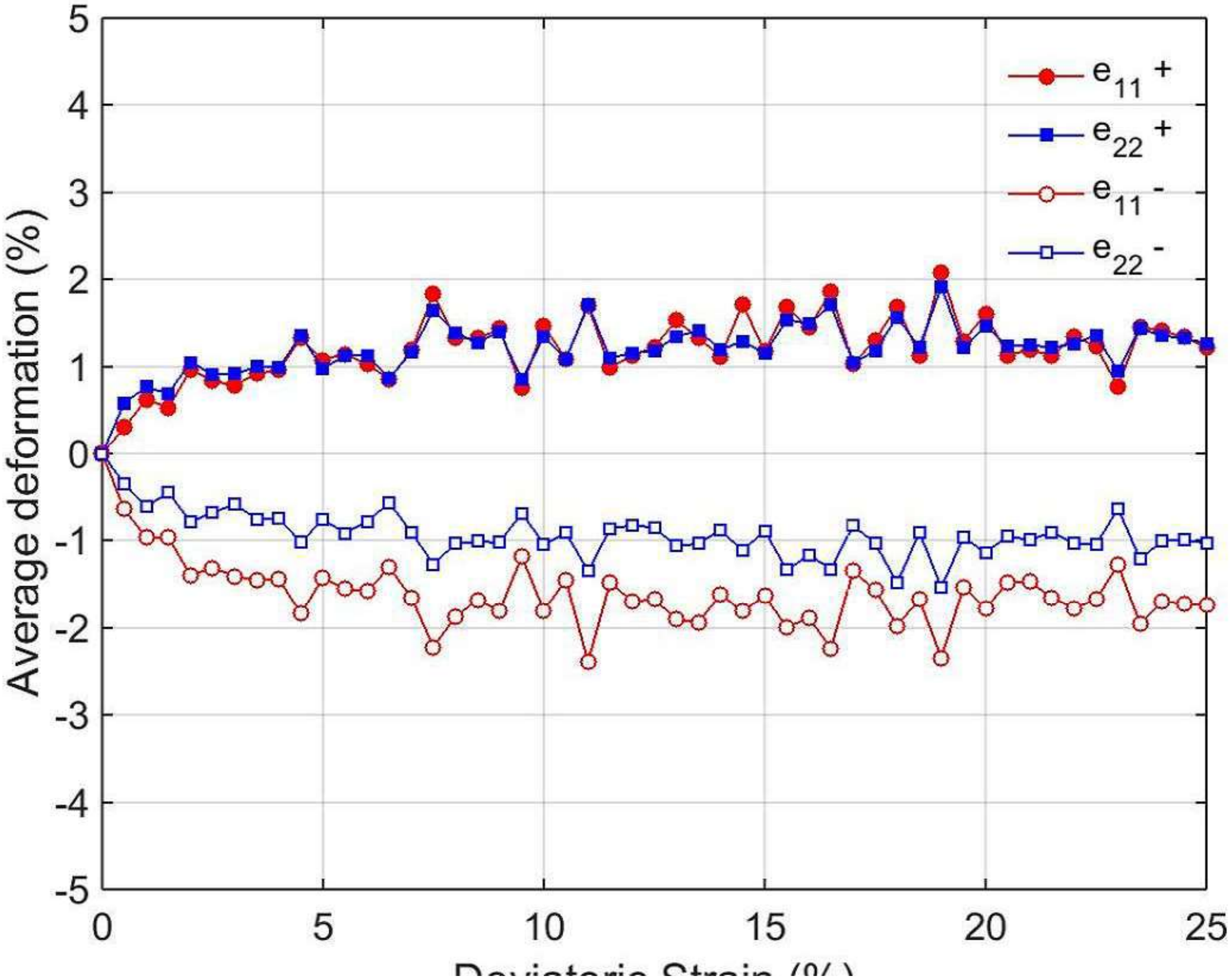
Average deformation (%)
5
4
3
2
1
0
-1
-2
-3
-4
-5
0
5
10
15
20
25
e11 +
e22 +
e11 -
e22 -

Figure

Click here to download Figure Fig-19c-3.pdf